https://ntrs.nasa.gov/search.jsp?R=20180003129 2020-05-09T19:06:04+00:00Z

MNRAS **000**, 1–17 (2017) Preprint 31 October 2017 Compiled using MNRAS LaTeX style file v3.0

Feeding the fire: Tracing the mass-loading of 10^7 K galactic outflows with O VI absorption

J. Chisholm[1⋆], R. Bordoloi[2†], J.R. Rigby[3] and M. Bayliss[2]
[1] *Observatoire de Genève, Université de Genève, 51 Ch. des Maillettes, 1290 Versoix, Switzerland*
[2] *MIT Kavli Institute for Astrophysics and Space Research, 77 Massachusetts Ave., Cambridge, MA 02139, USA*
[3] *Observational Cosmology Lab, NASA Goddard Space Flight Center, 8800 Greenbelt Rd., Greenbelt, MD 20771, USA*

arXiv:1710.06857v2 [astro-ph.GA] 29 Oct 2017

31 October 2017

ABSTRACT
Galactic outflows regulate the amount of gas galaxies convert into stars. However, it is difficult to measure the mass outflows remove because they span a large range of temperatures and phases. Here, we study the rest-frame ultraviolet spectrum of a lensed galaxy at $z \sim 2.9$ with prominent interstellar absorption lines from O I, tracing neutral gas, up to O VI, tracing transitional phase gas. The O VI profile mimics weak low-ionization profiles at low velocities, and strong saturated profiles at high velocities. These trends indicate that O VI gas is co-spatial with the low-ionization gas. Further, at velocities blueward of -200 km s^{-1} the column density of the low-ionization outflow rapidly drops while the O VI column density rises, suggesting that O VI is created as the low-ionization gas is destroyed. Photoionization models do not reproduce the observed O VI, but adequately match the low-ionization gas, indicating that the phases have different formation mechanisms. Photoionized outflows are more massive than O VI outflows for most of the observed velocities, although the O VI mass outflow rate exceeds the photoionized outflow at velocities above the galaxy's escape velocity. Therefore, most gas capable of escaping the galaxy is in a hot outflow phase. We suggest that the O VI absorption is a temporary by-product of conduction transferring mass from the photoionized phase to an unobserved hot wind, and discuss how this mass-loading impacts the observed circum-galactic medium.

Key words: ISM: jets and outflows, galaxies: evolution, galaxies: formation, ultraviolet: ISM

1 INTRODUCTION

Supernovae, stellar winds, cosmic rays and high-energy photons from high-mass stars accelerate gas out of star-forming regions as a galactic outflow (Heckman et al. 1990, 2000; Veilleux et al. 2005). Removing gas from galaxies stops runaway star formation by controlling the amount of gas converted into stars (Larson 1974; White & Frenk 1991; Hopkins et al. 2014), which may establish the observed star formation history of the universe (Madau et al. 1998; Springel & Hernquist 2003; Oppenheimer & Davé 2006).

While studies have established that outflows are ubiquitous in star-forming galaxies at all redshifts (Heckman et al. 1990, 2000; Pettini et al. 2002; Veilleux et al. 2005; Martin 2005; Rupke et al. 2005b; Weiner et al. 2009; Rubin et al. 2014; Bordoloi et al. 2014; Heckman et al. 2015; Bordoloi et al. 2016b; Chisholm et al. 2016a), the amount of mass ejected by outflows–the mass outflow rate–is challenging to constrain. Galactic outflows are diffuse, making them difficult to observe with emission lines outside of the local universe (Westmoquette et al. 2009; Sharp & Bland-Hawthorn 2010; Arribas et al. 2014). Typically, studies use metal absorption lines to probe the gas along the line-of-sight, which provides kinematic and column density information. However, converting these measurements into a mass outflow rate requires assumptions about the geometry, ionization structure, and metallicity of the outflow. These assumptions add up to a factor of ten uncertainty to most observed mass outflow rates (Murray et al. 2007; Chisholm et al. 2016a).

Most galactic outflow studies focus on warm gas at approximately 10^4 K because this gas phase has strong absorption and emission lines in the rest-frame ultraviolet and optical. However, galactic outflows are multiphase phenomena. Dense molecular outflows are observed in the local universe (Weiß et al. 1999; Matsushita et al. 2000; Leroy et al. 2015; Walter et al. 2017), with molecular mass outflow rates comparable to the neutral mass outflow rate, and up to 1.3 times larger than the star formation rate (Chisholm & Matsushita 2016). At the other end of the temperature range, X-ray observations of low redshift galaxies reveal that a pervasive large-scale wind fluid, with a temperature greater than

⋆ Contact email: John.Chisholm@unige.ch
† Hubble Fellow

© 2017 The Authors

10^7 K, dominates the thermal and kinetic energy of outflows (Griffiths et al. 2000; Strickland & Stevens 2000; Strickland & Heckman 2009). These molecular and hot winds may contain at least as much mass and energy as the 10^4 K phase; studies focusing only on warm outflows likely underestimate the total mass outflow rate.

Determining the mass outflow rate is additionally complicated by interactions between the different outflowing phases. Phase transitions convert molecular gas to atomic (Leroy et al. 2015), and photoionized gas is further ionized into the hot wind fluid (Strickland & Stevens 2000; Chisholm et al. 2016b), producing a shifting ionization structure. Consequently, a given outflow phase can dominate the mass and energy budget of an outflow at a given radius, velocity, or time. Strickland & Stevens (2000) find that most of the soft X-rays from the local starburst M 82 are produced when mass transfers from cooler phases into the hotter wind. These regions are called mass-loading regions because they feed most of the mass into the hot wind fluid (Mac Low et al. 1989; Suchkov et al. 1996; Strickland & Heckman 2009).

The hot wind can only be probed by X-ray observations, and only the nearest starbursts are bright enough to be observed in X-rays. Alternatively, the hot wind can be studied by observing gas that is temporarily created during mass-loading. With a cooling time of 1 Myr, "transitional" gas is short-lived because it sits near the peak of the cooling curve ($\sim 5 \times 10^5$ K; Spitzer 1956) and it must be observed shortly after it is created. The O VI 1032Å doublet is one of the few observable tracers of this transitional gas.

Observations of the O VI doublet are challenging because the transition is in the rest-frame far-ultraviolet (FUV), and must be observed from space for local galaxies. Complicating the situation, the high resolution configuration of the Cosmic Origins Spectrograph on the *Hubble Space Telescope* cannot observe the O VI doublet in local galaxies. The Far Ultraviolet Spectroscopic Explorer (FUSE) studied the O VI region in 16 galaxies, finding the O VI absorption line to have a velocity centroid that is 30 km s^{-1} more blueshifted than warm gas tracers, like C II, but with a similar maximum velocity (Heckman et al. 2001; Grimes et al. 2006, 2007, 2009). Few other studies have observed this important outflow phase, and the origin of O VI outflows is still unsettled.

In this paper, we analyze new spectroscopic observations of the O VI 1032Å absorption line from a gravitationally lensed, high redshift galaxy, SGAS J122651.3+215220, that is drawn from the Magellan Evolution of Galaxies Spectroscopic and Ultraviolet Reference Atlas (MEGaSaURA). The moderate resolution MEGaSaURA spectra provide unprecedented far-ultraviolet wavelength coverage, with absorption lines spanning a factor of 17 in ionization potential, allowing for a detailed comparison of the O VI line profile to low-ionization lines. First, we summarize the data reduction (Section 2) and analysis of the absorption lines (Section 3). Then, we compare the velocity-resolved O VI line profile to the low-ionization absorption lines (Section 4). In Section 5, we model the low-ionization lines with photoionization models to determine whether photoionization models reproduce the observed O VI. Finally, we discuss: O VI formation mechanisms (Section 6.1), upper limits for the column density and the mass outflow rate of each phase (Section 6.2), and the physical picture suggested by these observations (Section 6.3). With this analysis we explore what feeds the elusive and powerful 10^7 K hot wind.

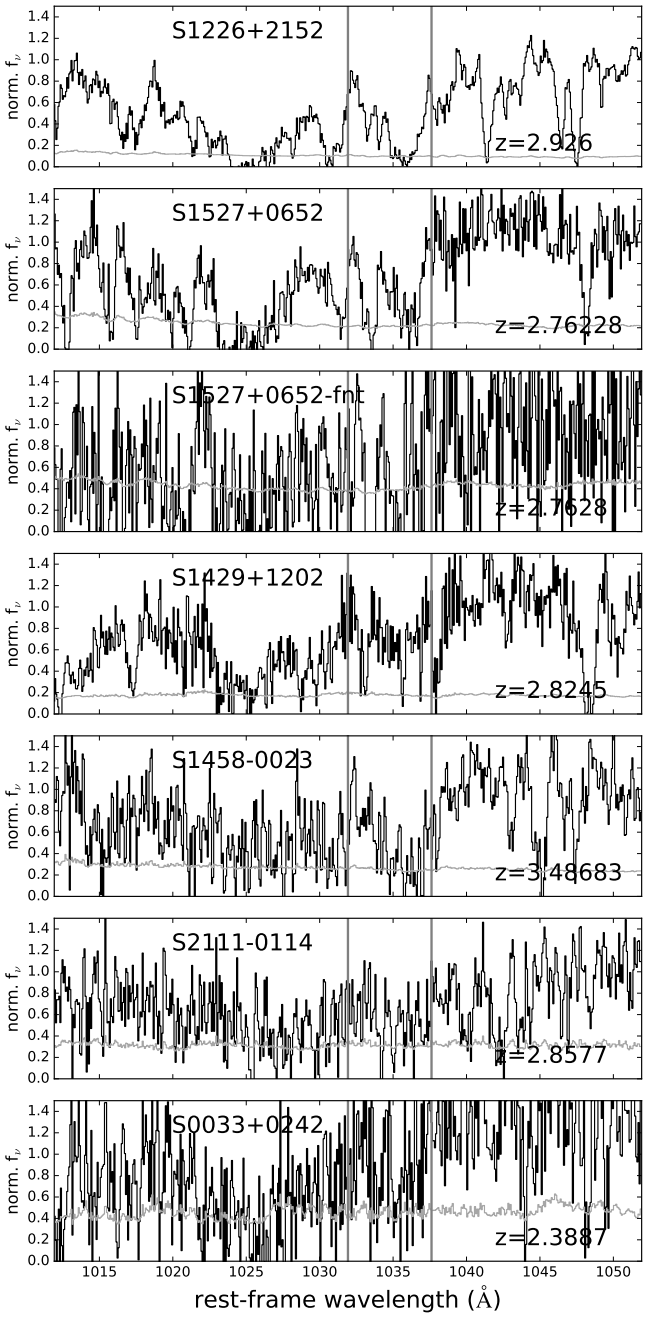

Figure 1. The O VI 1032Å region for six galaxies from the MEGaSaURA sample, arranged in descending order of their signal-to-noise ratio at the O VI 1032Å line, expect for J1527+0652-fnt which is a fainter knot from J1527+0652. The O VI 1032Å and 1038Å line are both marked by grey vertical lines. O VI 1032Å absorption is found in three of the four highest signal-to-noise observations (J1226+2152, J1527+0652, and J1458-0023).

2 MEGaSaURA DATA

The spectra used in this paper are drawn from Project MEGaSaURA: The Magellan Evolution of Galaxies Spectroscopic and Ultraviolet Reference Atlas (Rigby et al. 2017a). In short, some of the brightest gravitational lenses in the sky were observed with the Magellan Echellette (MagE) Spectrograph (Marshall et al. 2008) on the Magellan telescopes. The highest redshift galaxies within the MEGaSaURA sample have MagE

observations with rest-frame ultraviolet wavelengths between $850 \lesssim \lambda_r \lesssim 2200$ Å, suitable to analyze the O VI absorption line. The spectra were reduced using D. Kelson's Carnegie Python pipeline[1], and were corrected for Milky Way foreground reddening using the observed extinction from Pan-STARRS and 2MASS observations (Green et al. 2015), assuming the Milky Way extinction law (Cardelli et al. 1989).

In Fig. 1 we show the rest-frame spectra of the six MEGaSaURA galaxies with O VI 1032Å coverage. With the exception of J1429+1202, galaxies with SNR > 3 show broad O VI 1032Å absorption that is blueshifted from the stellar continuum, as demonstrated by the grey lines in Fig. 1. In a future paper, we will explore the outflow properties of the entire MEGaSaURA spectral data set, but here we focus on a single galaxy, SGAS J122651.3+215220 (hereafter J1226+2152; Koester et al. 2010), because the high signal-to-noise ratio (~ 10 at 1032Å) allows us to clearly define and characterize the O VI line profile. J1226+2152 has a redshift of 2.926 ± 0.0002, as measured from the [C III] 1907Å and C III] 1909Å nebular emission doublet (Rigby et al. 2017a). The total integration time for J1226+2152 was 12.42 hr, spread over multiple observing runs, with a final spectral resolution, as measured from night sky emission lines, of $R = 4010 \pm 170$ (75 ± 3 km s^{-1}). The median signal-to-noise ratio per resolution element was $SNR = 20$.

3 SPECTRAL ANALYSIS

3.1 Continuum fitting

The spectrum of J1226+2152 is observed ''down-the-barrel'' such that the ISM absorption lines are imprinted onto the stellar continuum. In this subsection we discuss how we fit and remove the stellar continuum to account for the shape and absorption lines of the background stars. We fit the stellar continuum twice: once for wavelengths greater than 1240Å, and once for wavelengths around the O VI doublet (1015-1045Å). The continuum must be fit twice because there are numerous intervening absorbers in the Lyα forest which can drive the stellar continuum fits if they are not properly masked.

Following Chisholm et al. (2015), we fit the stellar continuum redward of 1240Å using MPFIT (Markwardt 2009) with a linear combination of 10 single age (with ages between 1-40 Myr), fully theoretical STARBURST99 models (Leitherer et al. 1999, 2010) that use the Geneva stellar evolution models with high mass loss rates (Meynet et al. 1994), while simultaneously fitting for the stellar continuum extinction (E_s(B-V)) using a Calzetti extinction law (Calzetti et al. 2000). We allow for the five STARBURST99 stellar continuum metallicities (0.05, 0.2, 0.4, 1.0, 2.0 $Z_\odot$), and choose the best-fit model using a χ^2 test. The best-fit model is over-plotted on the observed data in Fig. 2 and has an E_S(B-V) of 0.15 ± 0.002 mag, a stellar metallicity of 0.2 $Z_\odot$, and a light-weighted age of 11 Myr. We cross-correlate the best-fit model with the data to determine the velocity offset between the observed stellar continuum and the STARBURST99 models. This velocity offset defines the zero velocity of the spectrum, also known as the systemic redshift. Further, we use the fitted STARBURST99 model as the ionizing source for the CLOUDY models in Section 5.2.

[1] The pipeline can be found at http://code.obs.carnegiescience.edu/mage-pipeline

The O VI doublet, at wavelengths of 1032Å and 1038Å, is in an extremely complicated spectral region. O VI in the atmosphere of hot massive stars produces strong P-Cygni profiles (Leitherer et al. 1999), while there is strong Lyβ 1026Å absorption from both the background stars and the foreground interstellar medium. Additionally, there are many strong interstellar metal absorption lines, such as Si II 1020Å, O I 1025Å, C II 1036Å, and O I 1039Å, that blend with the O VI profiles. Determining the continuum in this region is challenging, but without a physically motivated continuum the broad Lyβ or stellar O VI P-Cygni profiles may be mistaken for high-velocity O VI (see Fig. 3).

We fit the O VI continuum region of J1226+2152 using a simultaneous model of empirical STARBURST99 models and a Lyβ Voigt profile. We mask, by hand, regions of possible intervening absorbers (gray regions in Fig. 3) and interstellar metal lines. For simplicity, and because the Calzetti law is not defined at these wavelengths, we do not account for reddening. The resultant fit is shown by the red line in Fig. 3, where the zero-velocity of the O VI doublet is marked by two vertical dashed lines. The weaker O VI 1038Å line is severely blended by the interstellar C II 1036Å and O I 1039Å absorption lines; we cannot use the O VI 1038Å line for this reason.

3.2 Comparing the O VI absorption profile to low-ionization profiles

The stellar continuum-normalized O VI 1032Å line profile is shown in all panels of Fig. 4 as the black line, with low-ionization lines overplotted in colors. The O VI 1032Å line is broad (full width at half maximum of 150 km s^{-1}) and blueshifted relative to the stellar continuum by an average of -246 km s^{-1}, with deep absorption at blue velocities.

In Fig. 4 we show transitions of varying strength and ionization potential. The covering fraction and optical depth govern the line profiles, and we use the equivalent width ratios of doublet absorption lines to demonstrate whether a transition is optically thick. If the weaker line in a doublet is optically thin then the ratio of the two equivalent widths will be equal to the ratio of the two transition's $f\lambda$, where f is the f-value of the line. Meanwhile, if the line is optical thick, the ratio of the two equivalent widths will be 1. The equivalent width ratio between Si IV 1393Å and Si IV 1402Å is 1.6, implying that the Si IV line is not strongly saturated because the $f\lambda$ ratio is 2.0. Similarly, in Fig. 5 we show the Si II 1808Å, 1527Å, and 1260Å transitions which have f-values of 0.0025, 0.13, and 1.2, respectively. The Si II 1260Å transition is saturated over the entire profile, while the Si II 1808Å profile is only marginally detected (3σ). The Si II 1527Å line resides between these two extremes.

Singlets, like O I 1302Å and Al II 1670Å, cannot have their saturation levels diagnosed, but Fig. 4 shows that these lines have similar profiles to Si IV 1393Å. Meanwhile, lines like C II 1335Å, Si III 1206Å, and Si II 1260Å are nearly black at all velocities, implying that they are saturated at all velocities. Consequently, Fig. 4 shows four strong lines (Si III 1206Å, Si II 1260Å, C II 1335Å, and C IV 1548Å) and four relatively weak lines (O I 1302Å, Si IV 1393Å, Al II 1670Å, and Al III 1863Å).

By visual inspection of Fig. 4, we compare the O VI and low-ionization line profiles. The shape and depth of the velocity profile is insensitive to the ionization potential of the line: the Si II 1260Å profile has a lower ionization potential than the Si IV 1393Å line, but the Si II profile extends to larger velocities. At velocities between $+100$ and -200 km s^{-1}, the shape and depth of the O VI profile resembles those of the weak lines like O I 1302Å,

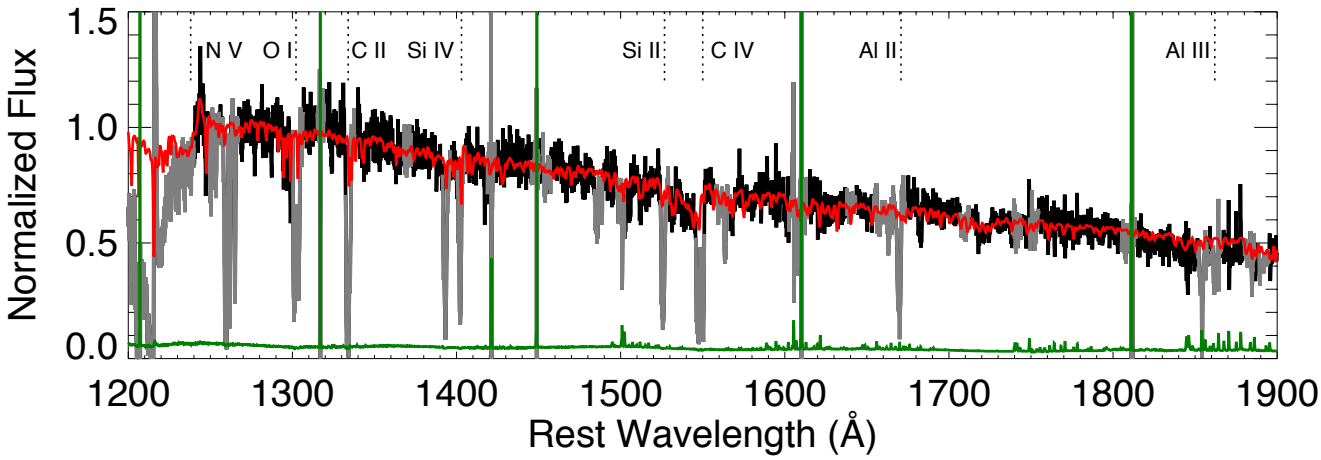

Figure 2. Observed spectrum (in F_λ) of J1226+2152 in black for the restframe wavelength regime between 1200–1900Å, with the error array included in dark green. Gray areas are masked out of the stellar continuum fitting to avoid interstellar and intervening absorption lines. Over-plotted in red is the STARBURST99 stellar continuum fit to the data (see Section 3.1). The stellar continuum fit establishes the continuum level and the zero-velocity (systematic) of the spectrum. The best fit stellar continuum model has a light-weighted age of 11 Myr, a stellar metallicity of 0.2 $Z_\odot$, and stellar extinction of E(B-V) = 0.15 mag. Interstellar absorption lines used in the paper are marked by dashed lines in the upper portion of the plot.

Table 1. Quantities derived from the interstellar metal absorption lines of J1226+2152. Column 1 indicates the transition, column 2 gives the ionization potential, column 3 gives the velocity at half the equivalent width ($v_{\rm cen}$), column 4 gives the velocity at 90% of the continuum on the blue portion of the profile (v_{90}), column 5 gives the rest-frame equivalent width (W_r), column 6 gives the measured apparent optical depth column density calculated using equation 10 (N), and column 7 gives the column density of the best-fit CLOUDY model. Transitions that are blended with other transitions are denoted by a ''b''. Possibly saturated lines are marked with an ''s''. The N V 1243Å line is reported as an upper limit because the line is not detected (ND; see Fig. 7). Transitions used in the CLOUDY modeling are denoted with a ''c''.

Line	Ionization Potential	$v_{\rm cen}$	v_{90}	W_r	log(N)	CLOUDY log(N)
	[eV]	[km s^{-1}]	[km s^{-1}]	[Å]	[log(cm^{-2})]	[log(cm^{-2})]
(1)	(2)	(3)	(4)	(5)	(6)	(7)
Si I 1845.51	8.2	-16 ± 117	-35 ± 10	0.24 ± 0.03	13.28 ± 0.13	10.82
O I 1302.17	13.6	-175 ± 8	-429 ± 14	1.32 ± 0.05	15.62 ± 0.11	16.13^c
Fe II 1608.46	16.2	-158 ± 7	-363 ± 36	0.64 ± 0.06	14.85 ± 0.03	14.34
Si II 1808.00	16.3	-93 ± 31	-168 ± 4	0.25 ± 0.08	15.57 ± 0.14	15.13
Si II 1304.37	16.3	-175 ± 5^b	^{b}	1.18 ± 0.12^b	15.23 ± 0.02^b	15.13
Si II 1526.71	16.3	-162 ± 12	-466 ± 9	1.63 ± 0.16	15.15 ± 0.08	15.13^c
Si II 1190.42	16.3	-236 ± 4^b	-631 ± 17^b	1.91 ± 0.19^b	$> 15.0^s$	15.13
Si II 1193.29	16.3	-169 ± 4	-450 ± 17	1.50 ± 0.15	$> 15.0^s$	15.12
Si II 1260.42	16.3	-201 ± 10	-585 ± 40	1.78 ± 0.25	$> 14.46^s$	15.13
Al II 1670.79	18.8	-196 ± 14	-448 ± 8	1.51 ± 0.15	13.88 ± 0.04	13.81^c
S II 1250.58	23.3	-110 ± 49	-127 ± 7	0.24 ± 0.03	15.61 ± 0.05	14.95
C II 1334.53	24.4	-125 ± 8	-505 ± 33	2.43 ± 0.24	$> 15.52^s$	16.37
Al III 1854.72	28.4	-109 ± 25	-369 ± 9	1.12 ± 0.11	14.06 ± 0.06	14.91
Al III 1862.79	28.4	-104 ± 31	-254 ± 13	0.80 ± 0.08	14.15 ± 0.04	13.91^c
Si III 1206.51	33.5	-184 ± 98	-650 ± 13	2.80 ± 0.28	$> 14.40^s$	15.39
Si IV 1393.76	45.1	-130 ± 9	-455 ± 10	1.85 ± 0.18	14.68 ± 0.03	14.78
Si IV 1403.77	45.1	-153 ± 11	-394 ± 15	1.15 ± 0.12	14.69 ± 0.04	14.78^c
C IV 1548.20	64.5	-194 ± 55^b	-478 ± 150	^{s,b}	$> 15.10^{s,b}$	15.60
C IV 1550.77	64.5	-146 ± 18^b	^{b}	^{s,b}	$> 15.23^{s,b}$	15.60
N V 1242.80	97.9	$--$	$--$	ND	< 14.25	10.89
O VI 1031.91	138	-246 ± 11	-532 ± 2	2.46 ± 0.25	15.35 ± 0.05^s	0

Al II 1670Å, Al III 1863Å, and Si IV 1393Å; while at velocities blueward of -200 km s^{-1}, the O VI profile resembles the strong Si II 1260Å and C II 1335Å lines. Consequently, the O VI profile has two regimes: a low-velocity regime that follows the weak lines, and a high-velocity regime that follows the saturated lines. This indicates that the O VI profile is sensitive to the optical depth at low-velocities, but it is saturated at high-velocities. We return to this in Section 4.

3.3 Velocity-resolved apparent optical depth profiles

The strength of a line is approximated by the optical depth (τ), a proxy for the column density. The apparent optical depth ($\tau_{\rm AOD}$; Savage & Sembach 1991) gives a lower limit of τ because the covering fraction (C_f), resolution effects, and saturation can increase the actual τ (see Section 4). In the upper panel of Fig. 6, we explore how the $\tau_{\rm AOD}$ of four ions evolves with velocity. The satu-

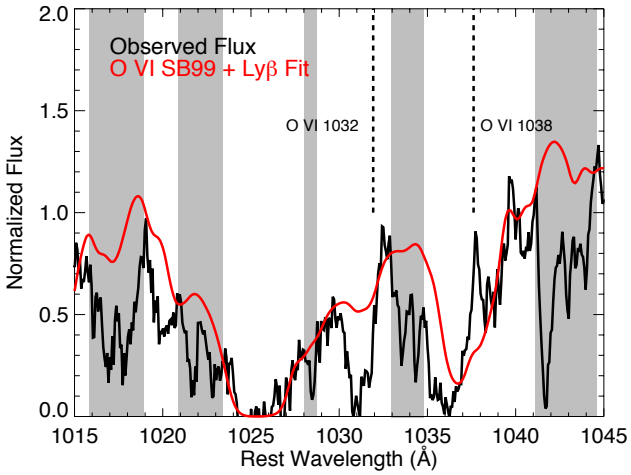

Figure 3. The simultaneous STARBURST99 and Lyβ fit (red line) to the O VI region (black line) for the lensed galaxy J1226+2152. The zero-velocity, as determined by the redshift from the stellar continuum fitting, of the O VI 1032Å and 1038Å lines are denoted by dashed vertical lines. The O VI 1038Å line is heavily blended by nearby interstellar O I and C II lines, and we do not use that line in our analysis. The STARBURST99 fit accounts for the stellar continuum and Lyβ contributions to establish the unity flux level of the O VI profile below. Gray regions show areas of intervening absorbers that were masked from the continuum fit.

rated C II 1334Å and Si II 1260Å distributions are similar, while the Al II 1670Å distribution is a factor of 2.3 smaller. The Al II $\tau_{\rm AOD}$ does not rise much above 1, while C II and Si II are above two for all velocities between 0 and -350 km s^{-1}, and decline collectively at bluer velocities.

The O VI 1032Å $\tau_{\rm AOD}$ follows the Al II $\tau_{\rm AOD}$ from 0 to -200 km s^{-1}, and rapidly increases at bluer velocities. At the highest velocities, the O VI profile declines on the same trajectory as the C II and Si II profiles. The velocity-resolved $\tau_{\rm AOD}$ follows the two-regime scenario for the O VI profile outlined above.

The two-regime behavior is emphasized when we sum the $\tau_{\rm AOD}$ with velocity (lower panel of Fig. 6). Again, the O VI $\tau_{\rm AOD}$ rapidly diverges from the Al II profile at velocities blueward of -200 km s^{-1} (marked by the vertical dashed line), and approaches the C II and Si II distributions. At -200 km s^{-1} the O VI profile shifts from behaving as a weak line (like Al II 1670Å) to behaving as a strong line (like C II 1335Å or Si II 1260Å). In Section 4 we use the weak Si IV doublet to explore a possible physical mechanism for these two regimes.

The similarity between the O VI and low-ionization line profiles indicates that the different ions are co-moving because they have similar absorption at similar velocities. Moreover, it appears that the O VI transition strengthens at velocities blueward of -200 km s^{-1}, and the profile declines in tandem with the strongest transitions at the bluest velocities. Since these lines all have different optical depths, the shared decline at high velocities is likely due to a declining covering fraction. The covering fraction relates the physical sizes of the outflow, consequently, the similar covering fractions indicate that the O VI is also co-spatial with low-ionization gas.

3.4 Velocities of photoionized and transitional gas

We measure the velocities for each transition in two ways (Table 1). The first way is the central velocity ($v_{\rm cen}$), which is defined as the velocity at half of the total equivalent width of the line. $v_{\rm cen}$ is influenced by zero-velocity absorption (Chisholm et al. 2015), or by resonance emission lines (Prochaska et al. 2011a; Scarlata & Panagia 2015), therefore we also measure the velocity at which the line profile reaches 90% of the continuum on the blue-side of the profile (v_{90}). We estimate the errors on each quantity by producing 1000 realizations of the data by multiplying each observed pixel by a random number drawn from a Gaussian distribution centered on zero with a standard deviation equal to the error on the flux.

The velocities of the individual transitions confirm what we saw by eye in Fig. 4: strong transitions (Si II 1260Å, Si III 1206Å, and C II 1334Å) have large v_{90}, while weaker transitions (Al II 1670 and Si IV 1402Å) have significantly smaller v_{90}. Since O VI follows the weaker lines at low velocity and the stronger lines at high velocity, the $v_{\rm cen}$–which is weighted by the equivalent width–shifts bluewards. Therefore, O VI has the largest $v_{\rm cen}$ of any transition, even though other transitions have larger (Si II, Si III), or comparable (C II), v_{90}. The two-regime behavior of O VI may explain why previous studies, that only quantized the outflow velocity with $v_{\rm cen}$, found a larger $v_{\rm cen}$ for O VI than the low-ionization lines, even though the O VI absorption profiles did not extend bluer than the low-ionization lines (Figure 3 of Heckman et al. 2001; Grimes et al. 2009).

3.5 The non-detection of N V

Before preceding, one notable exception to these observations is the N V 1243Å line (see Fig. 7). Strangely, interstellar N V 1243Å is not detected in absorption in the spectrum of J1226+2152, even though N V has an ionization potential between the observed O VI and C IV transitions. N V 1243Å is a relatively strong transition (f-value of 0.08) arising from a cosmologically abundant element (N/H $= 7.5 \times 10^{-5}$; Jenkins 2009), indicating that there is negligible gas in the N V ionization state. N V is also rarely detected in lower redshift galactic outflows (Chisholm et al. 2016a), providing a clue about the ionization structure of galactic outflows. We will use the N V non-detection in Section 6.1 when we explore how O VI is produced.

4 MODELING THE ABSORPTION LINE PROFILES

In the previous section we found that the O VI line profile has two regimes bisected at -200 km s^{-1}: the depth of the O VI line matches the weak lines at redder velocities, while the depth matches the strong lines at bluer velocities. Here we model the line profiles to explore the origin of this two-regime behavior.

4.1 Velocity-resolved optical depths and covering fractions

There are two degenerate ways to change the depth of an absorption profile: C_f and τ. Both these quantities change with velocity to produce the observed profile. C_f is the fraction of the total area of the background continuum source that the absorbing gas covers. A C_f of 1 means that the gas completely covers the background stellar continuum, while a C_f of 0 means that the gas does not cover the background source. If τ is large, then the depth of the line is $1 - C_f$.

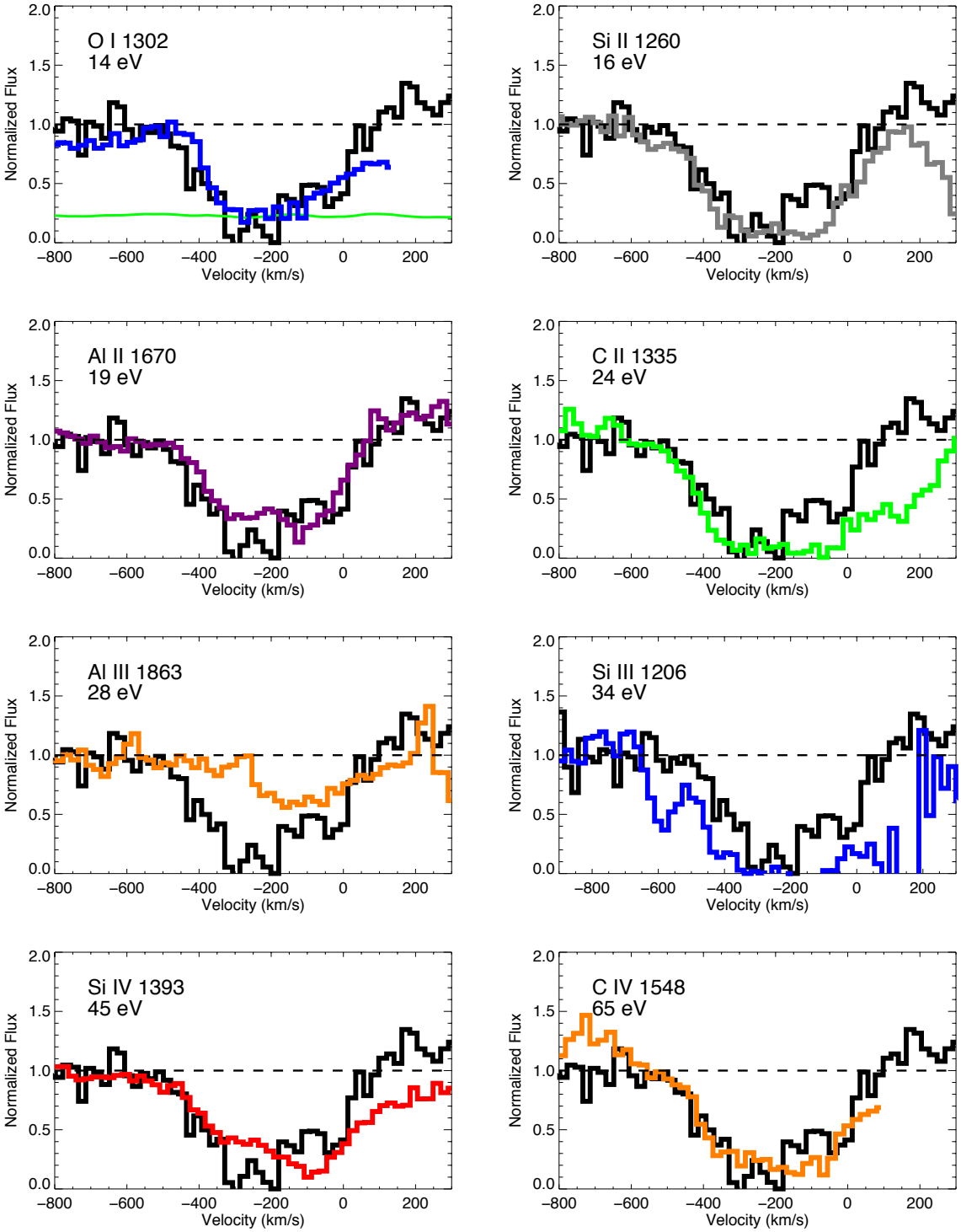

Figure 4. Comparison of the stellar continuum-normalized absorption profiles for various ISM metal absorption lines (in colors) with the O VI line profile in black in all the panels. The panels are ordered in terms of increasing ionization potential of the low-ionization transition. O I 1302Å, Al II 1670Å, Al III 1863Å, and Si IV 1393Å are not black at any portion of their line profiles, and are considered weak lines. Conversely, the Si II 1260Å, Si III 1206Å and C II 1335Å lines are nearly black over 400 km s^{-1}, and are considered strong lines. Note that the Si III 1206 Å line is close to the broad Lyα absorption line, and we fit a spline to further normalize the spectrum. The error array corresponding to the O VI region is shown in green in the top left panel (the O I panel). Blueward of -200 km s^{-1} the O VI profile is similar to the strong low-ionization absorption lines–like Si II, Si III and C II–while the depth and shape of the O VI profile redward of -200 km s^{-1} is similar to the weak lines–like Al II, Al III and O I.

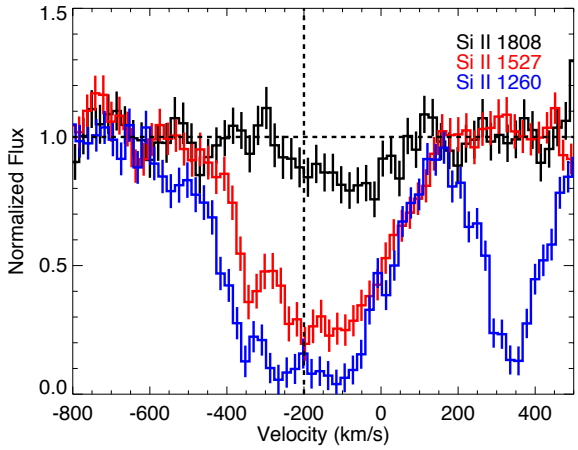

Figure 5. The Si II 1808Å (black), Si II 1527Å (red), and Si II 1260Å (blue) absorption profiles. The error bars show the 1σ flux errors. The Si II absorption lines have f-values of 0.0025, 0.13, and 1.22, respectively. There is an intervening absorber (detected with a doublet finding algorithm) at $+350$ km s^{-1} from the Si II 1260Å line. The marginal detection (3σ) of Si II 1808Å leads to a Si II column density of log(N[cm^{-2}])= 15.57 ± 0.14, consistent, within 2σ, with the Si II column densities measured from the Si II 1527Å line. The weak Si II 1808Å line is not significantly detected blueward of -200 km s^{-1} (vertical dashed line), which is the velocity where the photoionized density begins to rapidly decline (see Section 4.2).

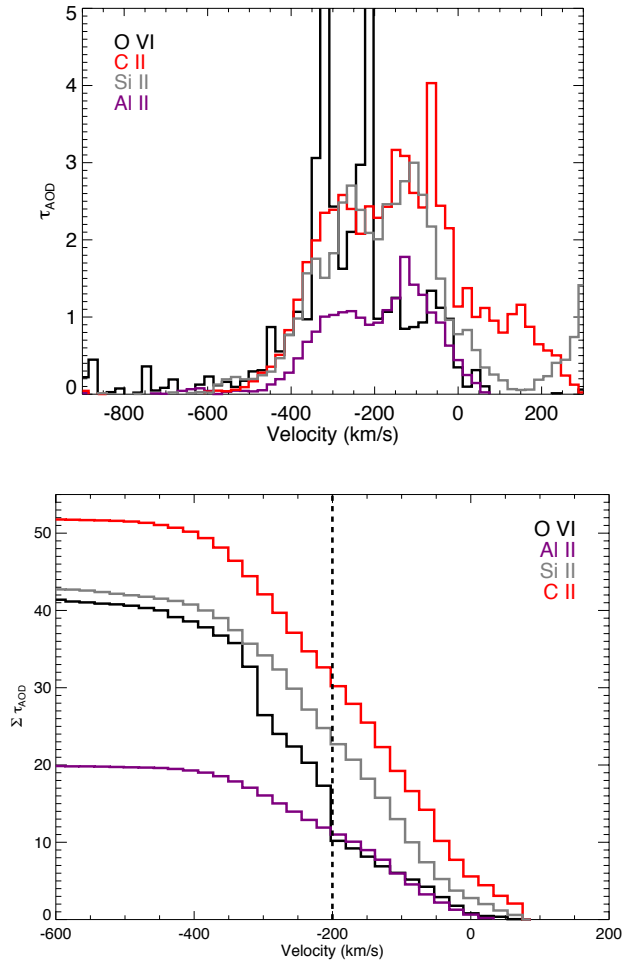

Figure 6. *Upper Panel:* Velocity-resolved apparent optical depth ($\tau_{\rm AOD}$) distributions for four transitions: O VI 1032Å (black line), C II 1335Å (red line), Si II 1260Å (gray line) and Al II 1670Å (purple line). The C II and Si II lines are saturated over the entire profile, while the Al II line is not. *Lower Panel:* Cumulative $\tau_{\rm AOD}$ distribution summed from positive velocities to negative velocities for the same ions as the upper panel. The O VI $\Sigma\tau_{\rm AOD}$ matches the Al II $\Sigma\tau_{\rm AOD}$ from 0 km s^{-1} to -200 km s^{-1} (marked by the dashed vertical line), while it matches the Si II and C II distributions at velocities blueward of -200 km s^{-1}.

The second way to change the depth of an absorption profile is through the optical depth, or approximately the column density (N). At τ greater than 3 the line becomes optically thick and C_f completely sets the depth of the line. Meanwhile at lower optical depths some light passes through the gas, and the flux is no longer zero. Consequently, the depth of an absorption line is degenerate with both τ and C_f. The radiative transfer equation describes this degeneracy as:

$$F(v) = 1 - C_f(v) + C_f(v)e^{-\tau(v)} \tag{1}$$

where $F(v)$ is the continuum normalized flux transmitted through the gas at a particular velocity (v). The only way for $F(v)$ to approach zero is if $C_f(v)$ approaches 1 and $\tau(v) > 3$ ($e^{-3} = 0.05$), otherwise the line has residual flux. This is seen in Fig. 4 and Fig. 5 where the weak lines (O I 1302Å, Si II 1527Å, Al II 1670Å, and Si IV 1393Å) all have non-zero flux across their line profiles, while the strong lines (Si II 1260Å, C II 1335Å) have an average depth of 0.1 between 0 and -300 km s^{-1}, implying that $C_f(v) \approx 0.9$.

The degeneracy between C_f and τ is broken with a doublet from the same ionic species. With a doublet, equation 1 becomes a system of two equations where each line has the same C_f and their τ is related by the ratio of their f-values. The Si IV 1402Å and Si IV 1393Å doublet has a f-value ratio of 2. The system of equations exactly solves for C_f and τ in terms of the flux of the two transitions as

$$\begin{aligned} C_f(v) &= \frac{F_{\rm W}(v)^2 - 2F_{\rm W}(v) + 1}{{\rm F_S}(v) - 2{\rm F_W}(v) + 1} \\ \tau(v) &= \ln\left(\frac{C_f(v)}{C_f(v) + F_{\rm W}(v) - 1}\right) \end{aligned} \tag{2}$$

Where $F_W(v)$ is the flux of the weaker doublet line at a given velocity and $F_S(v)$ is the flux of the stronger line. We calculate the errors on $C_f(v)$ and $\tau(v)$ by preforming a Monte Carlo analysis at each velocity, similar to how we calculated the velocity errors.

Using equation 2, we solve for the Si IV C_f and τ at each velocity (Fig. 8). At very low velocities the τ and C_f are impacted by zero-velocity absorption and resonance emission (Prochaska et al. 2011a; Scarlata & Panagia 2015). To assess the contamination from the emission, we use the Si II* 1197Å non-resonant emission line to determine which velocities are contaminated by the emission. The Si II* line is narrow, with emission only within ± 50 km s^{-1}, therefore, we exclude those velocities from consideration (grey points in Fig. 8).

In the lower left panel of Fig. 8, $C_f(v)$ declines at velocities blueward of -40 km s^{-1} until velocities near -300 km s^{-1} where it increases from $\approx 70\%$ covered to fully covered, and then rapidly settles to zero coverage. The increase blueward of -300 km s^{-1} in C_f is observed in the Si II 1260Å, Si IV 1393Å, and Al II 1670Å profiles as a ''second component'' (Fig. 4).

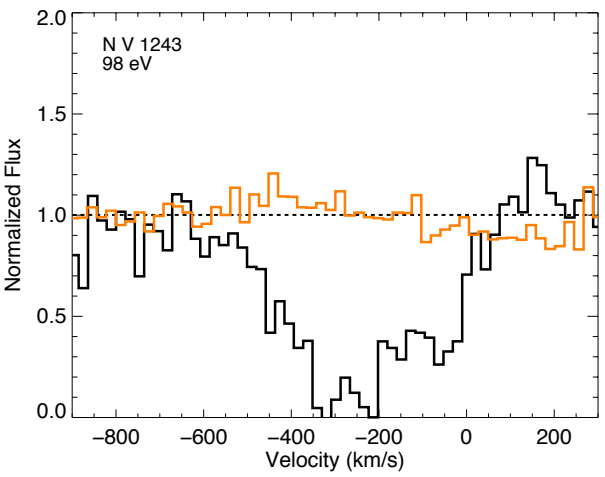

Figure 7. Comparison of the stellar continuum-normalized absorption profiles for the N V 1243Å transition (orange line) and the O VI 1032Å transition (black line). The dashed black line marks the unity flux level. The N V 1243Å line is not detected in the spectrum, placing an upper limit on the N V column density.

The Si IV $\tau(v)$ peaks at velocities near -175 km s^{-1}, and declines at velocities blueward of -200 km s^{-1} (upper right panel of Fig. 8). At the bluest velocities, the Si IV 1402Å line profile is set by both $C_f(v)$ and $\tau(v)$ because $\tau(v) < 3$. Meanwhile, stronger lines, like C II 1335Å and Si II 1260Å, still have $\tau(v) > 3$ at these velocities, and their line profiles do not change appreciably until velocities blueward of -350 km s^{-1} when $C_f(v)$ rapidly drops. The degeneracy between $\tau(v)$ and $C_f(v)$ dominates the line profiles of weak lines, while $C_f(v)$ determines the line profiles of strong lines.

4.1.1 An origin of the two-regime behavior of O VI

Fig. 8 illustrates why the O VI profile has two regimes. At low-velocities the O VI profile follows the τ dominated regimes of the weak lines, while at velocities blueward of -200 km s^{-1} O VI is optically thick and the line profile is determined by C_f. This split at -200 km s^{-1} is the same velocity where the Si IV τ begins to decline, indicating that the O VI τ increases as the Si IV τ decreases.

To illustrate this, we take the observed Si IV C_f from the lower left panel of Fig. 8 and correct the O VI column density for the partial coverage (bottom right panel of Fig. 8; see Section 5.1 for details on this correction). At redder velocities the Si IV and O VI column densities follow similar trends, but at bluer velocities the Si IV column density decreases as the O VI column density increases. The increased O VI column density means that O VI becomes a strong line, like Si II 1260Å or C II 1335Å, and the blue-wing of the O VI profile is now fixed by C_f. This also means that at bluer velocities the O VI line likely saturates, and the derived velocity-resolved column densities are lower limits. The transition of O VI from an optically thin line to an optically thick line naturally explains the two-regime O VI profile: at redder velocities the O VI profile matches the weak transitions whose profiles are governed by changes in τ at a nearly constant C_f, while at bluer velocities the O VI profile resembles the strong transitions whose profiles change as C_f changes. Similar behavior is also observed in other high signal-to-noise ratio spectra in the MEGaSaURA sample (see J1527+0652 in Fig. 1).

4.2 A model describing the Si IV profile

Above, we found that the O VI column density rises as the Si IV column density declines. This suggests a relationship between the two phases of gas that we discuss further in Section 6.3. To gain insight into this connection, here we explore a physical model for the Si IV profile. This model was fully introduced in Chisholm et al. (2016b), and we refer the reader there for details on its derivation.

Physically, C_f varies with velocity because the absorbing clouds cover a changing amount of the total area of the background stellar continuum. This change is caused by geometric dilution–the clouds occupy a smaller fraction of the total area at larger radii–or because the size of the outflowing clouds change with velocity (Martin & Bouché 2009; Steidel et al. 2010). A simple geometric model relates changes in C_f to changes in the area occupied by the absorbing gas as a power-law with

$$C_f(r) = C_f(R_\mathrm{i}) \left(\frac{r}{R_\mathrm{i}}\right)^\gamma \tag{3}$$

where $C_f(\mathrm{R_i})$ is the covering fraction at the initial radius ($\mathrm{R_i}$) and γ is an unknown power-law exponent. Introducing normalized coordinates simplifies this relation, such that

$$C_f(x) = C_f(R_\mathrm{i}) x^\gamma \tag{4}$$

where $x = r/R_\mathrm{i}$. If the outflowing clouds remain the same size, C_f decreases with radius as a power of $\gamma = -2$ as the projected area increases as r^2. For a local star-forming galaxy, NGC 6090, Chisholm et al. (2016b) find that the C_f evolves as r$^{-0.8}$, less rapidly (lower γ) than expected from geometric dilution, but consistent with the outflow adiabatically expanding as it accelerates.

Changes in $\tau(v)$ come from two sources: changes in the density of the absorbers ($n(v)$) and the velocity distribution of the absorbers. A power-law describes the radial change in density, such that

$$n\,(r) = n_0 \left(\frac{r}{R_\mathrm{i}}\right)^\alpha = n_0 x^\alpha \tag{5}$$

where $\alpha = -2$ if the outflow is a mass-conserving spherical outflow, and $\alpha < -2$ if gas is removed from the outflow, or if the geometry significantly deviates from a spherical outflow (Fielding et al. 2017). Possible ways to remove gas from the outflow are ionizing the outflow to a different ionization state (Chisholm et al. 2016b) or if gas exits the outflow as a galactic fountain (Leroy et al. 2015). Again for NGC 6090, Chisholm et al. (2016b) find $\alpha = -5.7$, possibly because a hot outflow destroys the low-ionization gas and incorporates it into a hotter outflow.

Changing how the gas is distributed in velocity also changes $\tau(v)$. Often times Gaussian or Lorentzian velocity distributions are assumed, where the absorbers are spread out in velocity space due to their thermal (or turbulent) motions (Rupke et al. 2005a; Martin & Bouché 2009; Chen et al. 2010). However, these assumed velocity distributions do not describe galactic outflows in which the radial velocity gradient broadens the observed line profile. The outflow velocity gradient measures how rapidly the velocity changes with radius (dv/dr). If dv/dr is large, then the velocity of the outflow rapidly changes while only traveling a short radial distance. In this case, there are fewer total absorbers per velocity interval, and correspondingly the optical depth is lower. Conversely, a small dv/dr means that the outflow accelerates gradually with radius, piling more absorbers into each velocity interval. The Sobolev approximation (Sobolev 1960) defines τ in terms of the density and radial velocity gradient as

$$\tau(v) = \frac{\pi e^2}{\mathrm{mc}} f \lambda_0 n(v) \frac{dr}{dv} \tag{6}$$

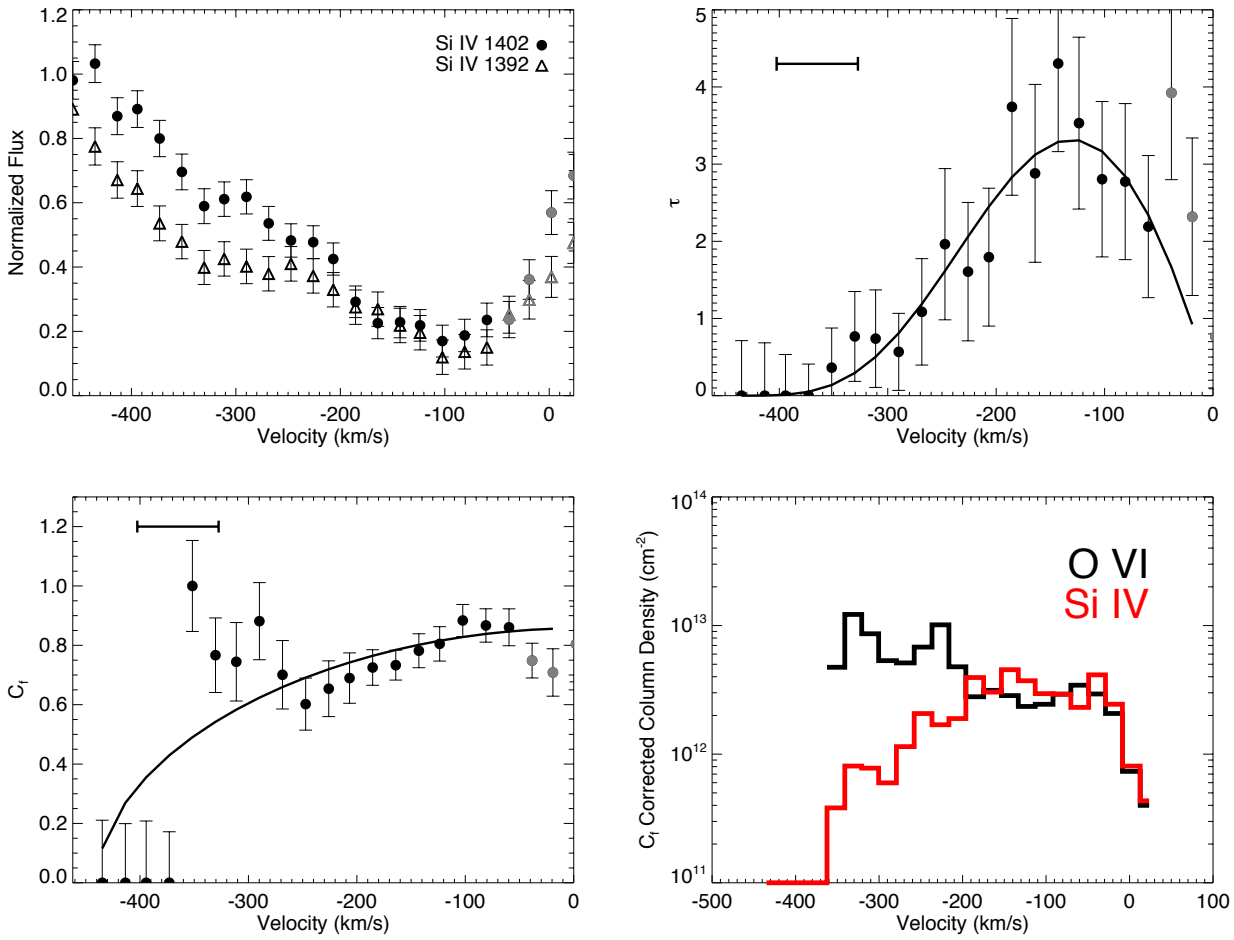

Figure 8. Si IV profile fits. The upper left panel shows the Si IV 1402Å (filled circles) and Si IV 1393Å (triangles) profiles. The grey points are excluded from the fit due to contamination with resonance emission, as determined from the Si II* emission line. These profiles are used to calculate the velocity-resolved optical depth (τ; upper right panel) and covering fraction (C_f; lower left panel) using the radiative transfer equation (equation 2). We simultaneously fit a model to the C_f and τ distributions (equation 8) as shown by the solid lines in the two panels. In the lower right panel we use the observed Si IV C_f to correct the O VI (black) and Si IV (red) column densities for partial coverage, assuming that O VI and Si IV have similar C_f. At velocities blueward of -200 km s^{-1} the column density profiles diverge: the Si IV column density rapidly decreases while the O VI column density increases. The velocity resolution of 75 km s^{-1} is indicated by bars in the τ and C_f panels.

Table 2. Parameter estimates to the simultaneous τ and C_f fit of equation 8. Column 2 gives the optical depth normalization (τ_0), Column 3 gives the maximum covering fraction ($C_f(R_{\rm i})$), Column 4 gives the radial velocity-law exponent (β; equation 7), Column 5 gives the density power-law exponent (α; equation 5), and Column 6 gives the covering fraction exponent (γ; equation 4). The first row gives the estimates for the high redshift galaxy J1226+2152, while the second row shows the parameters for the local star-forming galaxy NGC 6090 (Chisholm et al. 2016b).

Galaxy	τ_0	$C_f(R_{\rm i})$	β	α	γ
J1226+2152	8.1 ± 2.5	0.86 ± 0.03	0.53 ± 0.10	-6.3 ± 1.7	-0.53 ± 0.13
NGC 6090	4.8 ± 1.4	1.0 ± 0.04	0.43 ± 0.07	-5.7 ± 1.5	-0.82 ± 0.23

where f is the f-value of the transition, λ_0 is the transition's rest wavelength, and m is the mass of the electron.

The velocity gradient is not known a priori, but we fit for it from the shape of $\tau(v)$ and $C_f(v)$ (Fig. 8). Analytic relations for the acceleration (or deceleration) of outflows find that the velocity changes with radius (Murray et al. 2005) as a β-velocity law (Lamers & Cassinelli 1999), such that

$$v = v_\infty(1 - \frac{R_{\rm i}}{r})^\beta = v_\infty(1 - \frac{1}{x})^\beta \tag{7}$$

where v_∞ is the maximum observed velocity (440 km s^{-1} for Si IV 1402Å). It is important to note that equation 7 does *not* require that the outflow accelerates: a negative β produces a decelerating profile. Rather, we fit for β from the Si IV 1402Å profile, while al-

lowing for β values between -5 and $+5$. The shape of $\tau(v)$ and $C_f(v)$ define whether the outflow is accelerating or decelerating. In Chisholm et al. (2016b), NGC 6090 has $\beta = 0.43$, which is consistent with a r^{-2} force law opposed by gravity, such as ram pressure (Chisholm et al. 2016b).

The derivative of equation 7 defines the velocity gradient, allowing for the C_f (equation 4) and τ (equation 6) distributions to be rewritten in terms of the normalized velocity ($w = v/v_\infty$) as

$$\begin{aligned} \tau\,(w) &= \frac{\pi e^2}{mc} f \lambda_0 \frac{R_\mathrm{i}}{v_\infty} n_{4,0} x^\alpha \frac{dx}{dw} = \tau_0 \frac{w^{1/\beta-1}}{\beta(1-w^{1/\beta})^{2+\alpha}} \\ C_f(w) &= \frac{C_f(R_i)}{(1-w^{1/\beta})^\gamma} \end{aligned} \tag{8}$$

where $\mathrm{n}_{4,0}$ is the Si IV density at R_i. The constant preceding the τ distribution is rewritten as

$$\tau_0 = \frac{\pi e^2}{\mathrm{mc}} f \lambda_0 \frac{\mathrm{R_i}}{\mathrm{v}_\infty} \mathrm{n}_{\mathrm{H},0} \chi_{\mathrm{Si4}} (\mathrm{Si/H}) \tag{9}$$

Where $\mathrm{n}_{\mathrm{H},0}$ is the total hydrogen density at the base of the outflow, χ_{Si4} is the Si IV ionization fraction, and Si/H is the silicon to hydrogen abundance. With the ionization models of Section 5.2, we solve for R_i in equation 9 to derive the initial radius of the outflow.

We use MPFIT (Markwardt 2009) to fit for the five parameters in equation 8 (τ_0, $C_f(R_\mathrm{i})$, β, α, γ; see Table 2). In Table 2 we compare the fitted parameters to the local star-forming galaxy NGC 6090 (Chisholm et al. 2016b). β, α and γ describe the radial variation of C_f (equation 4), density (equation 5), and velocity (equation 7); these exponents are similar to local galaxies. This implies that the outflow properties of high and low redshift galaxies vary similarly with radius (Rigby et al. 2017b). Intriguingly, the $C_f(R_\mathrm{i})$ of 0.86 is roughly consistent with the maximum depth of the Si II 1260Å and C II 1335Å lines being near 0.1 in normalized flux units, further emphasizing that these lines are optically thick and dominated by C_f.

These models illustrate many interesting features of the Si IV profiles. For instance, the rapid acceleration ($\beta = 0.53$) of the outflow means that the outflow initially does not travel a large distance in each velocity interval. This rapid acceleration means that the dynamical time, as defined by the velocity profile (equation 7), is only ~ 0.2 Myr. Since the density decreases with radius, not velocity, the rapid acceleration ensures that the density does not decrease appreciably in each redder velocity interval. In fact, equation 5 implies that at -200 km s^{-1} the density is still 20% of the initial density. This allows the Si IV and Al II lines to remain strongly detected, but the weaker Si II 1808Å transition is undetected blueward of -200 km s^{-1} (Fig. 5). By the time the outflow reaches -300 km s^{-1} the Si IV density is now 1.5% of the original density, and at -400 km s^{-1} the density is 1×10^{-5} times the original density. At these densities the Si IV optical depth drops below the detection threshold, and the line is no longer observed. Meanwhile, the Si II 1260Å line has an f-value 5 times larger and an ionization correction that is twice that of Si IV 1402Å (see Section 5.2), implying that the Si II τ is roughly 10 times larger than the Si IV τ. From Fig. 8, the Si II 1260Å line is still optically thick at -300 km s^{-1}, with τ near 10. Even at large velocities, Si II 1260Å is optically thick and the profile is determined by C_f.

Finally, equation 4 explains why C_f evolves slowly at redder velocities. The rapid acceleration means that the outflow does not travel far in these velocity intervals. At bluer velocities the outflow covers more distance (dv/dr is smaller), decreasing the C_f and shaping the line profiles of the strong lines (Si II 1260Å, C II 1335Å, and O VI 1032Å).

At the moderate spectral resolution of the MEGaSaURA data, it is important to check that the resolution does not dramatically affect the measured C_f. To do this, we make a synthetic line profile using the fitted properties from Table 2, and then convolve the profile to the 75 km s^{-1} resolution of the MEGaSaURA data. We then measure the deepest portion of the profile and find that it increases by 0.09 normalized flux units. This increase is within the median C_f error of 0.13 normalized flux units between -400 and 0 km s^{-1} (see Fig. 8), therefore we conclude that the impact of the resolution is within our quoted C_f errors.

5 PHOTOIONIZATION MODELING

In the previous section, we used the line profiles to show that the O VI column density increases as the Si IV density declines, even though the two phases are co-spatial. This suggests that the O VI column density is decoupled from the Si IV column density, and the low-ionization gas is created by a different mechanism than the transitional gas. In Chisholm et al. (2016a), the low-ionization equivalent widths are consistent with predictions from CLOUDY photoionization models (Ferland et al. 2013), if the observed stellar continuum is the ionizing source. Here, we use the observed column densities and the stellar continuum fit to predict the column densities of the individual transitions. This tests whether the O VI is also photoionized, or if separate ionization mechanisms produce the observed O VI and photoionized gas.

5.1 Measuring observed column densities

The observed column density (N) of a given transition is the product of the outflow's metallicity, density, and ionization structure. To characterize the ionization structure, we measure the integrated column density of each transition using a modified apparent optical depth method (Savage & Sembach 1991) which accounts for non-unity covering of the source (see Section 4.2) as

$$N = \frac{3.77 \times 10^{14}\ \mathrm{cm}^{-2}}{\lambda_0[\text{Å}] f} \int \ln\left(\frac{C_f(R_\mathrm{i})}{C_f(R_\mathrm{i}) + F_\mathrm{o}(v) - 1}\right) \mathrm{d}v \tag{10}$$

where λ_0 is the rest wavelength of each transition, f is the oscillator strength of each transition, and $F_\mathrm{o}(v)$ is the continuum-normalized flux. We use the $C_f(R_\mathrm{i})$ from the Si IV 1402Å transition because many of these lines are singlets, and we cannot derive their velocity-resolved C_f distributions. Additionally, Chisholm et al. (2016a) show that C_f does not vary appreciably from transition to transition. This can be seen in Fig. 4 where C_f appears to be near 0.9 for the strong transitions (where $C_f = 1 - F$ for saturated lines). The errors are calculated similar to the velocity errors, and a 10% uncertainty is included, in quadrature, to account for the continuum normalization uncertainty. The values are given in Table 1.

Many of these transitions could be heavily saturated. Al III 1862Å and Si IV 1402Å are doublets, and their equivalent width ratios diagnose saturation (discussed in Section 3.2). The observed Al III and Si IV doublet ratios are 1.4 and 1.6, while their f-value ratios are both 2. This implies that these transitions are not heavily saturated.

The wavelength coverage and sensitivity of the MEGaSaURA data also allows us to measure lines that are not typically measured (see Pettini et al. 2002, for another example). The Si II 1808Å line has an f-value of 0.0025, and is unsaturated. At a signal-to-noise ratio near 10, we marginally detect this line above the

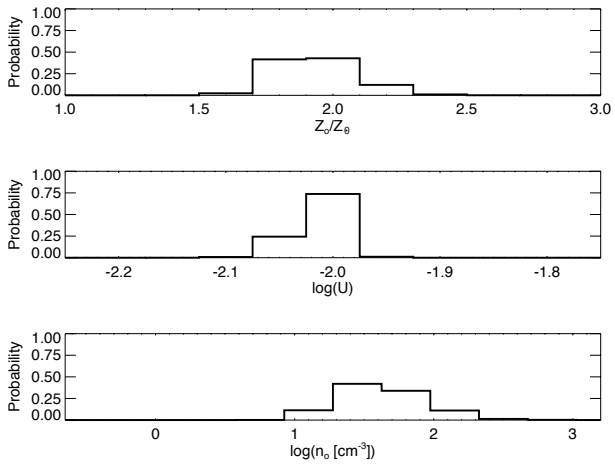

Figure 9. Probability density functions for the three parameters used to generate the CLOUDY models: outflow metallicity (Z_o), ionization parameter (U), and hydrogen density at the base of the outflow ($n_{H,0}$). The expectation values for Z_o, log(U), and $n_{H,0}$ are 1.94 $Z_\odot$, -2.01 dex, and 42 cm^{-3}.

Table 3. CLOUDY parameter grid used to estimate the ionization parameter (log(U)), hydrogen density at the base of the outflow ($n_{H,0}$) and metallicity of the outflow (Z_o). The second column gives the parameter range used in the Bayesian analysis and the third column gives the number of bins for each parameter. The expectation values and standard deviations of the parameters for J1226+2152 are given in the fourth column, and the fifth column shows the estimates for NGC 6090, a local star-forming galaxy.

Parameter (1)	Range (2)	Bins (3)	Expected Value (4)	NGC 6090 (5)
log(U)	$-1.5 \rightarrow -2.5$ dex	21	-2.01 ± 0.02	-1.85
log($n_{H,0}$)	$-0.65 \rightarrow 3.2$ dex	12	42 ± 31 cm^{-3}	19 cm^{-3}
Z_o	$0.1 \rightarrow 3.0$ $Z_\odot$	16	1.94 ± 0.15 $Z_\odot$	1.6 $Z_\odot$

continuum noise (a 3σ detection; see Fig. 5). The logarithm of the Si II 1808Å column density is 15.57 ± 0.14 cm^{-2}, which is consistent, within 2σ, with the column density measured from Si II 1304Å and Si II 1526Å (see Table 1). The photoionization models of the next section rely on the uncertainties of the column densities, and large statistical uncertainties, like the errors we measure for Si II 1808Å, do not constrain the models. Therefore, we use the Si II 1526Å column density (as denoted by the ''c'' in Table 1), but note that the Si II lines could be marginal saturated.

5.2 Can photoionization models reproduce the O VI?

The ionization structure depends on the input energy that heats the gas as well as how efficiently the gas loses energy by radiatively cooling. This cooling depends on the density, temperature, and metallicity of the gas. Consequently, the observed ionization structure sensitively depends on the ionizing spectrum, the density of the outflow, and the metallicity of the outflow.

We characterize the O and B stars ionizing the outflow with the measured STARBURST99 stellar continuum from the wavelength regime redward of 1240Å. We then model the ionization structure of the outflows using CLOUDY, v13.03 (Ferland et al. 2013), models that use these O and B stars as the ionizing source. In CLOUDY, we use an expanding spherical geometry, with the density profile determined in Section 4.2, and the initial covering fraction ($C_f(R_i)$). By including the fitted density profile from Section 4.2, we incorporate the decreasing outflow density with increasing velocity, which creates the two-regime O VI behavior (Section 4.1.1). We use CLOUDY's H II abundances, with the Orion nebular dust grain distribution (Baldwin et al. 1991), to account for dust scattering and depletion of metals onto grains. We do not change the relative abundances (like α-enhancement, or Fe-enrichment), which may have second order effects. We then scale the abundances by constant factors to enrich or deplete the gas according to Table 3. We stop running CLOUDY once the temperature has dropped to 500 K, and include a cosmic ray background (Indriolo et al. 2007).

From a given set of ionization parameters (U), outflow metallicities (Z_o), and hydrogen densities at the base of the outflow ($n_{H,0}$); CLOUDY estimates the total integrated column densities of the various ions along the line-of-sight, which we compare to the observed column densities using Bayesian inference (Kauffmann et al. 2003; Brinchmann et al. 2004). We use the large grid of CLOUDY models from Table 3 to calculate the probability of each model, given the observed column densities, using the likelihood function of

$$L \sim \exp\left(-\chi^2\right) \tag{11}$$

where χ^2 is the chi-squared function of the observed O I 1302Å, Si II 1527Å, Al II 1670Å, Al III 1862Å, and Si IV 1402Å column densities. Note that the observed O VI is not included in these photoionization models because we are trying to predict the O VI column density, given the observed low-ionization column densities, to determine if the observed O VI can be produced by photoionization. We then marginalize over nuisance parameters to produce the probability density functions (PDFs) for each parameter (Fig. 9). We take the expectation values and standard deviations of each of these PDFs as the parameter estimates of log(U), Z_o and $n_{H,0}$ (Table 3).

We then produce a CLOUDY model using the expectation values from the Bayesian inference. This gives the abundances and ionization fractions of each ion. For instance, the CLOUDY model predicts that the neutral fraction of the outflow is 3%, the Si IV ionization fraction is 14%, and the gas phase Si/H abundance is $10^{-5.11\pm0.02}$. The errors on the abundances are calculated by creating CLOUDY models using the standard deviations of the individual parameters. Additionally, the model predicts that the dominant silicon ionization state is Si III (containing 55% of the total silicon), and the outflow has a total hydrogen column density of $10^{20.75\pm0.04}$ cm^{-2}. With these photoionization models, and the fitted τ_0 value, equation 9 solves for the initial radius of the outflow from the ionizing source of $R_i = 28$ pc. This result is marginally smaller than the 33-101 pc range found for local galaxies in Chisholm et al. (2017).

J1226+2152 has a stellar mass upper-limit of $< 10^{9.5}$ $M_\odot$ (Wuyts et al. 2012), and the derived Z_o of 1.94 ± 0.15 $Z_\odot$ is significantly larger than the expected ISM metallicity from the mass-metallicity relation. Local low-mass ($\sim 10^7$ $M_\odot$) dwarf galaxies have similarly enriched galactic outflows, relative to their ISM metallicities (Chisholm et al. in preparation), which is proposed to drive the steep-portion of the observed stellar mass-metallicity relationship because outflows remove a substantial fraction of the metals produced during star formation (Tremonti et al. 2004). Even if the photoionization modeling overestimates Z_o, the relative results presented below do not change because we adopt the same metallicity for both the photoionized and O VI phases. Further, decreasing

Z_o does not allow for the photoionization models to reproduce the observed O VI column densities.

The fitted CLOUDY column densities have a median deviation of 0.2 dex from the observed values (see the last column of Table 1). The observed Si IV column densities, as well as the lower limits of the blended C IV lines, are consistent with the CLOUDY model, while O VI is not produced at all (see Table 1). Given the observed stellar continuum and the observed low ion column densities, the CLOUDY models do not produce nearly enough O VI to match the observations. Another ionization mechanism must produce the observed O VI.

6 DISCUSSION

6.1 How is the O IV created?

Since the photoionization models are unable to create nearly enough O VI, we explore possible alternative mechanisms to produce this transitional gas. The observations provide four constraints:

(i) O VI has a large integrated column density of $10^{15.35}$ cm^{-2} with velocity-resolved O VI densities near 2-10 $\times$ 10^{12} cm^{-2} km^{-1} s (Fig. 8).

(ii) N V is not detected, with upper limits of the N V to O VI ratio of log(N(N V)/N(O VI)) < -1.2 (see Section 3.5 and Fig. 7).

(iii) C IV and Si IV column densities are consistent with the column densities from the photoionization models, implying that the mechanism that creates the O VI produces negligible Si IV and C IV.

(iv) Low-ionization lines (like O I, Si II, Al II, etc.) have column densities consistent with the photoionization models.

Below we explore two excitation mechanisms that satisfy these four constraints. These two mechanisms are not an exhaustive list of ways to create O VI (see Spitzer 1996; Indebetouw & Shull 2004; Wakker et al. 2012, for reviews), but the above constraints eliminate many other mechanisms. Turbulent mixing layers between hot and cool gas, for example, require a log(N(N V)/N(O VI)) near -0.5 (Slavin et al. 1993; Kwak & Shelton 2010), which is inconsistent with constraint (ii) above. Additionally, collisional ionization equilibrium (Sutherland & Dopita 1993), galactic fountain models (Shapiro & Benjamin 1991), and shock models (Allen et al. 2008) do not satisfy constraint (iv) (Chisholm et al. 2016a).

Here, we explore two mechanisms that do satisfy the four criteria above. The two models explain opposite phenomena: cool gas evaporating into a hot medium (Section 6.1.1) and cool gas condensing out of a hot medium (Section 6.1.2). In the next two subsections we explain the two mechanisms and explore their implications for the ionization fractions of the transitional outflow. We stress that both models have many unconstrained parameters, and rather than trying to derive estimates of the total transitional gas, we maximize the values to predict upper limits. These models must be considered order of magnitude estimates, rather than precise calculations.

6.1.1 *Conductive evaporation*

Thermal conduction transfers thermal energy from a hot ($> 10^7$ K) wind to cooler gas, heating and evaporating the cool gas (McKee & Cowie 1977). As the interaction time increases, conduction heats more of the cool gas. This decreases the total amount of cool gas, while increasing the amount of hot and transitional gas (Indebetouw & Shull 2004). In this case, the O VI is short-lived as the hot outflow further heats the transitional gas to higher temperatures, and the O VI is only observed during this brief transition period.

Many studies explore the evaporation of cool gas by conduction with different assumptions for the direction of the hot flow and the orientation of the magnetic fields (McKee & Cowie 1977; McKee & Ostriker 1977; Ballet et al. 1986; Borkowski et al. 1990; Brüggen & Scannapieco 2016). These studies typically find log(N(N V)/N(O VI)) between -1.1 and -1.4, and log(N(C IV)/N(O VI)) between -0.4 and -1 (Indebetouw & Shull 2004). Further, these models predict O VI column densities per velocity interval between 7 and 14 $\times 10^{12}$ cm^{-2} km^{-1} s, in agreement with the C_f corrected column densities observed in Fig. 8. While a different physical situation, conductive interfaces also occur in a supernovae driven blastwave and produce similar results (Weaver et al. 1977; Slavin et al. 1993; Shelton 1998).

Borkowski et al. (1990) model a time-dependent plane-parallel conductive interface between a hot flow and cooler gas. This model computes the column densities of high-ionization lines like Si IV, C IV, N V, and O VI as a function of time, magnetic field orientation, and the physical conditions of the hot wind. In these models the O VI column density starts with a negligible column density and reaches a saturation level after $\sim 10^5$ years, which is similar to the observed 0.2 Myr dynamical time of the outflow. Using Equation 4 from Borkowski et al. (1990), parameters of the hot wind from Chevalier & Clegg (1985), and assuming that the magnetic field is parallel to the conduction front; we maximize the total hydrogen in the conductive interface, with a value of 2×10^{19} cm^{-2} km^{-1} s. This implies that our observed O VI is 1×10^{-4} times the total hydrogen, and the total integrated hydrogen column density is 8×10^{21} cm^{-2} in the conductive interface. Again, these estimations are upper limits because the values are maximized, but these values allow us to compare upper limits of the transitional gas to the photoionized gas in Section 6.2.

6.1.2 *Cooling Flow*

When hot gas interacts with cool gas, energy flows from the hot gas to the cool gas. If this interaction drops the hot gas temperature to near 5×10^5 K, the hot gas radiatively cools and rapidly transitions through temperatures corresponding to O VI.

Recent cooling flow models successfully relate the observed column densities to the line-widths of O VI and N V (Heckman 2002; Bordoloi et al. 2016a). These models predict that the total O VI column density increases with the line width, approaching values near 10^{15} cm^{-2} for the broadest lines. Using the observed O VI line width of 650 km s^{-1} and the column density of $10^{15.35}$ cm^{-2}, the cooling flow model of Bordoloi et al. (2016a) predicts the column densities of the other transitions. Table 4 indicates that the log(N(N V)/N(O VI)) and log(N(C IV)/N(O VI)) ratios are near -1.4 and -0.7, respectively. Summing up the total oxygen predicted, we find an O VI ionization fraction of 0.8%, a total oxygen column density of 3×10^{17} cm^{-2}, and a total hydrogen column density of 4×10^{20} cm^{-2}, using the metallicity of the photoionized gas.

6.2 Which phase dominates the outflow?

Now that we have explored the creation of the O VI gas, we ask: how does the total transitional phase compare to the photoionized

Table 4. Estimated column densities (N; in units of cm^{-2}) of five different ions from the Bordoloi et al. (2016a) cooling flow model. These values are estimated using an O VI line width of 650 km s^{-1}, an O VI column density of $10^{15.35}$ cm^{-2}, and a log(T) = 5.5 (Bordoloi et al. 2016a). This model implies that O VI is 0.8% of the total oxygen.

Si IV [cm^{-2}]	C IV [cm^{-2}]	N V [cm^{-2}]	O VII [cm^{-2}]	O VIII [cm^{-2}]
7×10^{13}	5×10^{14}	1×10^{14}	7×10^{16}	2×10^{17}

phase? We make this comparison first to the total column densities of the two phases (Section 6.2.1) and then to the mass outflow rates (Section 6.2.2).

6.2.1 *Comparing the column densities of the two phases*

The O I and O VI column densities are ideal to compare because they arise from the same element, and the only difference between the two transitions is their ionization states. O I is an unambiguous tracer of neutral gas because it has the same ionization potential as H I, and the O I ionization fraction is locked to H I through charge exchange. The measured O I column density is $10^{15.62}$ cm^{-2}, nearly a factor of 2 larger than the measured O VI column density. However, at blue velocities the O VI column density likely saturates, and the measured O VI column density could be consistent with the O I column density.

The O I transition only probes neutral gas, which the CLOUDY model suggests is only 3% of the total outflow. The wavelength coverage of the MEGASAURA data enables us to calculate the total silicon without assuming a model because it contains transitions from each photoionized silicon phase (Si I 1845Å, Si II 1527Å, Si III 1206Å, Si IV 1402Å; see Table 1). Adding up the observed column densities from these four transitions we find a lower limit of the total silicon column density of $10^{15.33}$ cm^{-2}, nearly equal to the total O VI column density. The silicon abundance in Section 5.2 provides a total photoionized column density of $10^{20.5}$ cm^{-2}, as compared to the $10^{21.9}$ and $10^{20.6}$ cm^{-2} found for the conductive interface and cooling flow models. Summing the observed silicon transitions implies that the total transitional gas has a column density roughly equal to, and at most 20 times larger than, the column density of the photoionized gas.

However, Si III is the dominant ion in the photoionized medium and it is heavily saturated. The CLOUDY model predicts a total hydrogen column density of $10^{20.75\pm0.04}$ cm^{-2}. This suggests that the photoionized column density is 2 and 0.1 times the size of the cooling flow and conductive interface models, respectively.

Dust along the line-of-sight extincts the observed stellar continuum. Assuming the dust-to-gas ratio scales with metallicity allows the hydrogen column density to be estimated from the measured extinction (Leitherer et al. 2002; Heckman et al. 2011). Using the relation from Calzetti et al. (2000), the total hydrogen column density is estimated from the UV extinction as

$$N_{\rm H} = \frac{2.4 \times 10^{21} E_{\rm gas}(B-V)}{Z} \tag{12}$$

where $E_{\rm gas}(B-V)$ is the gas phase extinction. We convert the measured stellar continuum extinction (0.15 mags) to $E_{\rm gas}(B-V)$ by dividing by 0.44 (Calzetti et al. 2000). Using the measured extinction and the derived outflow metallicity, we estimate a total hydrogen column density for the photoionized phase of $10^{20.64\pm0.03}$ cm^{-2}, where the uncertainty does not account for the extinction law. The inferred column density from the UV extinction is in agreement, within 2σ, with the total hydrogen column density from the CLOUDY models. This inferred photoionized column density is twice as large as the cooling flow column density and one-tenth the conductive interface column density. The exact comparison depends on how the O VI is created and the saturation of O VI. We qualitatively conclude that the photoionized column density is similar to the cooling flow column densities, and smaller than the conductive interface models. The transitional phase gas is a significant portion of the total outflow, and not including the transitional phase would underestimate the total amount of outflowing gas.

6.2.2 *Comparing the mass outflow rates of the two phases*

While deriving column densities does not require assumptions about the outflow geometry, the more fundamental quantity driving galaxy evolution is the mass outflow rate ($\dot{M}$). Here, we calculate $\dot{M}$ for both the transitional ($\dot{M}_{\rm tr}$) and photoionized ($\dot{M}_{\rm ph}$) phases to compare how the phases contribute to the total $\dot{M}$.

We calculate $\dot{M}_{\rm tr}$ using the observed O VI column density and the photoionized line profile fits. This fitting assumes that the O VI is co-moving with the photoionized phase, as suggested by their line profiles (see the discussion in Section 3.2). The O VI mass outflow rate ($\dot{M}_{\rm OVI}$) is calculated as

$$\dot{M}_{\rm OVI}({\rm r}) = \Omega C_f(r) v(r) m_{\rm OVI} N_{\rm OVI}(r) r \tag{13}$$

Where the radial covering fraction (equation 4), velocity law (equation 7), and radius (equation 9) are calculated in Section 3.2 (Table 2). Putting these relations into equation 13 gives $\dot{M}_{\rm OVI}$ as

$$\dot{M}_{\rm OVI}({\rm w}) = \Omega C_f(R_{\rm i}) v_\infty m_{\rm OVI} R_{\rm i} N_{\rm OVI}(w) \frac{w}{(1-w^{1/\beta})^{1+\gamma}} \tag{14}$$

Where $m_{\rm OVI}$ is 16 times the proton mass (the mass of oxygen atoms), w is the velocity normalized by v_∞ (532 km s^{-1} for O VI), and Ω is the solid angle covered by the outflow, which we assume is 4π. We use the C_f corrected O VI column density distribution ($N_{\rm OVI}(w)$) from Fig. 8. Since the O VI ionization fractions are highly uncertain (see Section 6.1), Fig. 10 shows $\dot{M}_{\rm OVI}$ (i.e. only the mass outflow rate of the O VI gas). The $\dot{M}_{\rm OVI}$ curve begins at a very low level and steadily increases as the velocity increases. Most of this increase happens between -180 and -320 km s^{-1} where $\dot{M}_{\rm OVI}$ increases by a factor of 30. These are the velocities where the O VI profile is likely saturated (see Fig. 6), and $\dot{M}_{\rm OVI}$ should be considered a lower-limit at these velocities.

Using the ionization corrections found in Section 6.1, we derive upper-limits of the total $\dot{M}_{\rm tr}$. $\dot{M}_{\rm tr}$ peaks at -320 km s^{-1} with values of 0.12 M$_\odot$ yr^{-1} and 0.009 M$_\odot$ yr^{-1} for the conductive interface and cooling flow models, respectively (Fig. 11). These estimates are for the total hydrogen mass outflow rate within the conductive interfaces or cooling flows, but do not include the mass in a hotter phase. It is important to stress that $\dot{M}_{\rm tr}$ likely continues rising at the bluest velocities, but the covering fraction corrected O VI column density is not defined past -340 km s^{-1} because the Si IV profile is no longer detected (see Fig. 8).

We follow Chisholm et al. (2016b) and calculate $\dot{M}_{\rm ph}$ as

$$\begin{aligned} \dot{M}_{\rm ph}(r) &= \Omega C_f(r) v(r) \rho(r) r^2 \\ \dot{M}_{\rm ph}(w) &= \Omega C_f(R_{\rm i}) v_\infty \mu {\rm m_p} n_{\rm H,0} R_{\rm i}^2 \frac{w}{(1-w^{1/\beta})^{2+\gamma+\alpha}} \end{aligned} \tag{15}$$

Now we use 1.4 times the mass of the proton (the effective mass

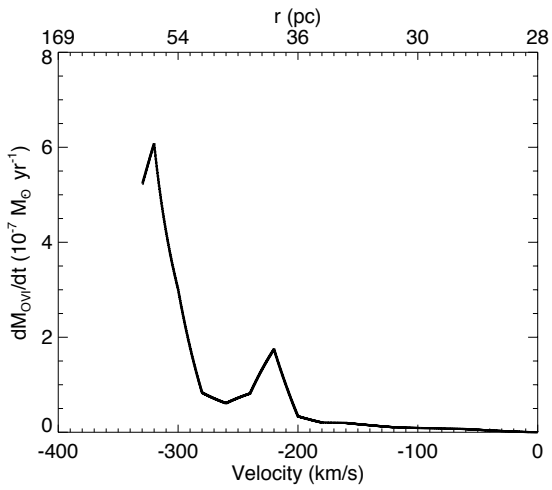

Figure 10. The velocity-resolved O VI mass outflow rate (dM_{OVI}/dt) in units of 10^{-7} $M_\odot$ yr^{-1}. This is calculated assuming that the O VI and Si IV are co-moving and co-spatial. The O VI mass outflow rate rises from $0.2\pm0.1\times10^{-7}$ $M_\odot$ yr^{-1} at -180 km s^{-1} to $6.1\pm3.0\times10^{-7}$ $M_\odot$ yr^{-1} at -320 km s^{-1}, increasing by a factor of 30 in 140 km s^{-1}. At these velocities O VI is likely saturated and the O VI mass outflow rate should be considered a lower limit. These are the same velocities that the Al II and Si IV optical depth profiles decline (Fig. 6 and Fig. 8). The upper x-axis gives the radial distance of the outflow from the ionizing source, using the initial radius and the velocity law (equation 7).

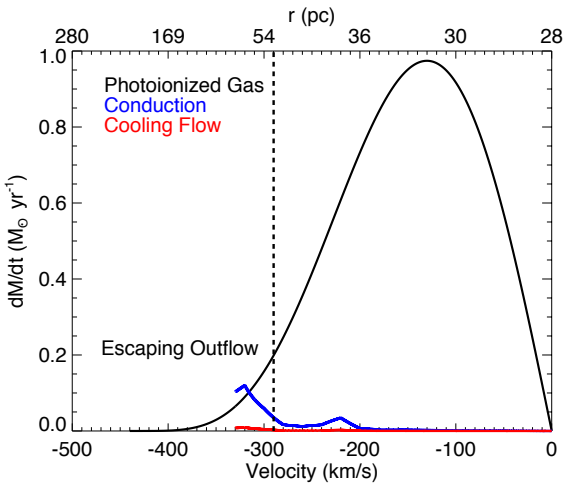

Figure 11. The model of the velocity-resolved photoionized mass outflow rate (dM/dt; black line), the mass outflow rate from a conductive interface (blue line), and a cooling flow (red line). All of these estimates are for the total hydrogen mass outflow rate in their respective phases. Both the blue and red lines should be treated as upper limits due to uncertain ionization corrections. The photoionized mass outflow rate peaks at 0.97 ± 0.39 $M_\odot$ yr^{-1}. The maximum mass outflow rate of the conductive interface model is 12% the peak of the photoionized gas. At -290 km s^{-1}, a dashed line represents the upper-limit of the escape velocity for J1226+2152. Any outflow blueward of this velocity is traveling fast enough to escape the gravitational potential of the galaxy. The photoionized outflow rapidly decreases at velocities above the escape velocity, while the transitional mass outflow rate dramatically increases and actually exceeds the photoionized outflow. The upper x-axis gives the radial distance of the outflow from the ionizing source, using the initial radius and the velocity law (equation 7).

per nucleon; μm_p) because we are calculating the total outflowing mass rather than just the O VI mass (we also use this value when calculating $\dot{M}_{tr}$ for the conductive interface and cooling flow models above). The parameters are taken from the photoionization modeling and the Si IV profile fitting, where v_∞ is -440 km s^{-1} for the Si IV line. $n_{H,0}$ in equation 15 is the total hydrogen density from the photoionization modeling in Section 5.2. Importantly, equation 15 has the exact same $C_f(r)$, $v(r)$, and R_i as equation 13. The difference between the two relations is the radial density distribution ($n(r)$ versus N_{OVI}) and the maximum velocity.

The maximum $\dot{M}_{ph}$ peaks at 1.0 ± 0.4 $M_\odot$ yr^{-1} and decreases at higher and lower velocities, where the $\dot{M}_{ph}$ errors are calculated using a Monte Carlo analysis of the input parameters from equation 15. The conductive interface $\dot{M}$ peaks at -320 km s^{-1}, with an upper limit of 0.12 $M_\odot$ yr^{-1} (blue line in Fig. 11), only 12% of the peak of $\dot{M}_{ph}$. The cooling flow model peaks at the same velocity with an upper limit of 0.009 $M_\odot$ yr^{-1} (red line in Fig. 11). The photoionized outflow is the chief contributor to $\dot{M}$ at the observed velocities.

$\dot{M}_{tr}$ rapidly rises at velocities blueward of -200 km s^{-1}, reminiscent of the velocity that splits the O VI profile into two regimes. The $\dot{M}_{tr}$ rises precisely at the same velocity as $\dot{M}_{ph}$ declines. In fact, at -320 km s^{-1} the $\dot{M}$ of the conductive interface model exceeds $\dot{M}_{ph}$, indicating that $\dot{M}_{tr}$ may dominate at bluer velocities. The continued acceleration of the transitional gas, saturation of the O VI, and the presence of a hotter undetected wind may further increase $\dot{M}_{tr}$ and provide the additional 0.9 $M_\odot$ yr^{-1} required to satisfy mass conservation. These requirements may indicate that the undetected hot wind component dominates the mass outflow rate at higher velocities.

The high velocity gas is the most important for galaxy evolution because this gas escapes the gravitational potential of the galaxy. Wuyts et al. (2012) place an upper-limit on the stellar mass of J1226+2152 at $\log(M_*) < 9.5$, which leads to an upper limit on the circular velocity of < 95 km s^{-1} (using the Tully-Fischer relation from Reyes et al. 2011). Heckman et al. (2000) approximate the escape velocity as three times the circular velocity, which means that an upper-limit for the escape velocity is < -290 km s^{-1}. At these velocities $\dot{M}_{ph}$ rapidly declines while $\dot{M}_{tr}$ increases; outflows above the escape velocity may entirely consist of hot and transitional gas. This likely means that studies focusing on cool photoionized gas to calculate the amount of mass escaping galactic potentials under-predict the total mass of high-velocity outflows. An analysis of the hotter phases are required to accurately determine this quantity.

6.3 A physical model explaining these observations

Here we synthesize the results of the past sections into a physical model that could explain the observations. First, we summarize the observations that our model tries to explain:

(i) The O VI line profile has two regimes, where it matches weak lines at redder velocities and strong lines at bluer velocities (see Fig. 4 and Fig. 6). Changes in covering fraction drive changes in the line profiles of strong lines, while changes in optical depth drive changes in the line profiles of weak lines. The division line for the O VI profile happens approximately at -200 km s^{-1}.

(ii) The covering fraction corrected Si IV column density drops sharply at bluer velocities (Fig. 8).

(iii) The covering fraction corrected O VI column density is flat at low velocities and increases at high velocities (Fig. 8). The

O VI profile transitions from being optical depth dominated at low velocities to covering fraction dominated at high velocities. The O VI column density starts increasing at -200 km s^{-1}.

(iv) $\dot{M}_{\rm ph}$ increases at low velocity and decreases at higher velocities as the density and covering fraction decline. As $\dot{M}_{\rm ph}$ decreases, $\dot{M}_{\rm OVI}$ increases by a factor of 30 (Fig. 10) and actually exceeds $\dot{M}_{\rm ph}$ at the highest observed velocities (Fig. 11).

(v) The O VI and photoionized gas are not created by the same mechanism. The CLOUDY models do not reproduce the observed O VI column densities (Table 1), but reasonably reproduce the photoionized gas. The N V non-detection indicates that the O VI is likely produced through conductive evaporation of the photoionized gas or through a cooling flow of a hotter outflow (Section 6.1).

Here we envision a simple model where a hot (>10^7 K) wind is incident on an ensemble of photoionized clouds (see a zoom-in of a single cloud in Fig. 12). The hot outflow accelerates the photoionized clouds from zero velocity to high velocities by ram pressure, as described by the velocity law in Section 4.2. At the interface of each cloud, heat transfers from the hot outflow to the photoionized clouds through conduction (Weaver et al. 1977), heating the outer layer of photoionized gas to high temperatures. The mass transfer reduces the density of the photoionized gas, while increasing the column density of the O VI and hot wind (lower right panel of Section 4.2). Geometric dilution, elongation from the ram pressure shock, and adiabatic expansion reduce the size and covering fraction of the photoionized clouds (Klein et al. 1994; Martin & Bouché 2009; Scannapieco & Brüggen 2015; Chisholm et al. 2016b; Brüggen & Scannapieco 2016). After about 0.2 Myr (the dynamical time of the photoionized clouds) conduction has evaporated most of the photoionized gas and incorporated it into the hot wind (Brüggen & Scannapieco 2016). The process increases the mass of the hot wind, while decreasing its average metallicity, temperature, and velocity (Thompson et al. 2016). The transfer of mass from the photoionized phase to the hot wind is often referred to as the mass-loading of the hot wind (Mac Low et al. 1989; Suchkov et al. 1996; Heckman et al. 2000; Strickland & Stevens 2000; Cooper et al. 2009; Strickland & Heckman 2009).

This model explains the observations in a number of ways. First, the O VI is co-spatial with the photoionized gas because the O VI only temporarily arises in the outer layer of the photoionized clouds (see Fig. 12). Second, to satisfy mass conservation, the photoionized mass must directly transfer to the hot wind. Therefore, as the photoionized density and $\dot{M}_{\rm ph}$ decreases, $\dot{M}_{\rm tr}$ and $\dot{M}_{\rm hot}$ must increase. This indicates that $\dot{M}_{\rm hot}$ should be substaintial at blue velocities.

Mass-loading of a hot wind with photoionized gas naturally explains the observed two-regime O VI line profile from Section 3.2. Before the hot wind interacts with the photoionized cloud, the cloud is at rest and the photoionized density is large (left panel of Fig. 12). Since photoionization produces negligible O VI, the O VI is optically thin at redder velocities. However, once the hot wind interacts with the photoionized cloud, conduction heats the cloud to temperatures briefly corresponding to O VI (right panel of Fig. 12). As the interaction continues, conduction forges more O VI by heating more photoionized gas. Consequently, while the hot wind accelerates the cloud, the weak low-ionization lines become optically thin as the O VI becomes optically thick. This is precisely what we observe in the lower right panel of Fig. 8. Once O VI saturates, the C_f of the clouds determines the shape of the profile. This is why the O VI profile closely follows the shape of other saturated lines (Si II and C II). Feeding photoionized gas into a hot wind creates the two-regime O VI line profile because at low velocities conduction has not acted long enough to produce appreciable O VI, while at high velocities conduction has produced enough O VI to saturate the transition.

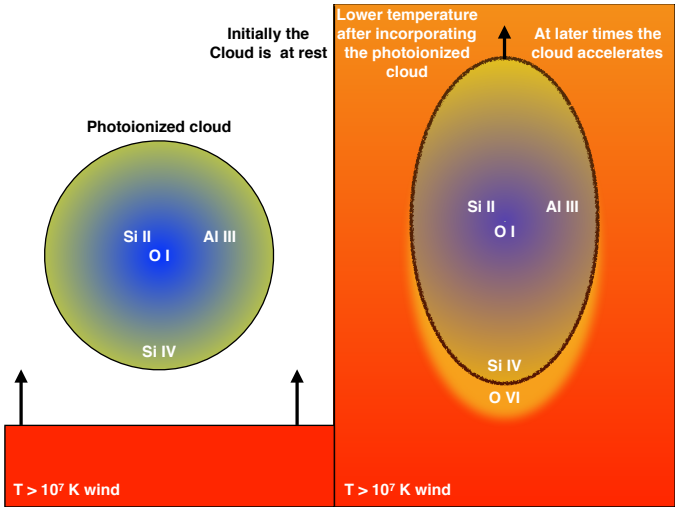

Figure 12. Cartoon of the physical picture that produces the O VI absorption. *Left Panel:* Initial conditions of a photoionized gas cloud at rest. A nearby starburst (not pictured) created a $T > 10^7$ K wind that propagates towards the photoionized cloud. Hypothetical locations of various observed ions are labeled. *Right Panel:* A time after the hot wind encountered the photoionized cloud. Ram pressure accelerates and elongates the cloud, while conduction between the hot outflow and the photoionized cloud evaporates the cloud to produce O VI at the interface. Energy from the hot outflow further heats and accelerates the O VI, which reduces the down-stream temperature of the hot wind. By incorporating the photoionized cloud, the down-stream outflow has an increased mass, but a lower temperature, velocity, and metallicity.

A prediction of this model is that as the outflow becomes more ionized (and consequently less dense), the velocity must increase to satisfy the continuity equation. The increased velocity causes the mass outflow rate of increasing ionization states to peak at bluer velocities (from photoionized gas to transitional gas in Fig. 11). Chisholm & Matsushita (2016) find that cold molecular outflows have lower outflow velocities than neutral outflows, and this model predicts that, if J1226+2152 has a molecular outflow, the molecular mass outflow rate should peak at velocities redward of -130 km s^{-1}.

6.3.1 *Does mass-loading of a hot wind impact the CGM?*

The small physical distance and the rapid destruction of photoionized clouds means that the observed photoionized clouds do not survive to travel into the circum-galactic medium (CGM). However, cool gas is observed in the CGM around galaxies (Tumlinson et al. 2011; Werk et al. 2014; Bordoloi et al. 2014; Borthakur et al. 2015; Prochaska et al. 2017). Here, we explore reconciling this issue by reforming the warm CGM through a radiative shock of the hot, mass-loaded wind (Wang 1995a,b; Thompson et al. 2016), and the implications that the proposed model of mass-loading has on the formation of the CGM.

At $1000 - 3000$ km s^{-1} (Chevalier & Clegg 1985; Bustard et al. 2016), the $T > 10^7$ K hot wind contains most of the outflowing energy. The hot wind travels out of the star-forming region where ambient gas is incorporated into the hot wind. After it is

mass-loaded, the hot phase travels outward with a reduced velocity because the acceleration and heating of the ambient gas consumes energy from the hot wind. Gravity, inter-galactic medium pressure, radiative cooling, and adiabatic expansion further decreases the velocity and temperature of the hot outflow until it reaches the peak of the cooling curve, which causes the hot outflow to radiatively shock and reform cool photoionized gas (Wang 1995a,b; Thompson et al. 2016).

Changing the initial composition, density, and temperature of the hot wind changes where the hot wind radiatively shocks. Thompson et al. (2016) predict that the cooling radius of the hot wind scales with the mass outflow rate and metallicity of the hot wind as $\dot{\mathrm{M}}_{\mathrm{hot}}^{-2.92}$ and $\mathrm{Z}_{\mathrm{hot}}^{-0.79}$, respectively. If we assume that the hot wind initially has the mass outflow rate of the transitional gas in Section 6.2.2 (1/8th the photoionized outflow rate) with the metallicity of pure supernovae ejecta ($\sim$ 5 $\mathrm{Z}_{\odot}$; Woosley & Weaver 1995), the addition of photoionized mass and metals will increase $\dot{\mathrm{M}}_{\mathrm{hot}}$ but decrease $\mathrm{Z}_{\mathrm{hot}}$, decreasing the cooling radius by a factor of 200 from 10 Mpc scales to 100 kpc scales. Without the mass-loading of cool clouds into the hot wind, the hot wind would not be massive enough to produce the observed metal-enriched CGM within 100 kpc of galaxies (Werk et al. 2014; Prochaska et al. 2017).

Further, whether the hot outflow shocks at all depends on the mass-loading. Thompson et al. (2016) show that there is a minimum ratio between $\dot{M}$ and SFR–the so called mass-loading factor–above which the hot wind will radiatively shock. If the mass-loading factor is lower than this minimum mass-loading factor, the hot wind does not lose enough thermal energy to reach the peak of the cooling curve, and never recreates the low-ionization gas observed in the CGM. Thompson et al. (2016) find that the minimum mass-loading factor ranges between $\dot{M}$/SFR=0.3−0.6.

Since the mass-loading factor of galactic outflows decreases with increasing stellar mass (Rupke et al. 2005b; Heckman et al. 2015; Chisholm et al. 2017), galaxies greater than $2-8\times10^{10}$ $\mathrm{M}_{\odot}$ generate outflows with mass-loading factors below the minimum mass-loading factor (Chisholm et al. 2017). Hot winds in high-mass galaxies never radiatively shock to produce O VI and low-ionization gas in the CGM. Instead the temperature of the hot wind remains above the peak of the cooling curve. Tumlinson et al. (2011) detect O VI absorption in 100% of the 19 galaxies with stellar mass less 4×10^{10} $\mathrm{M}_{\odot}$, but this detection rate drops to 52% for the 23 galaxies with stellar mass greater than 5×10^{10} $\mathrm{M}_{\odot}$ (note that these high-mass galaxies contain both star-forming and quiescent galaxies). Similarly, other studies find that the majority of O VI absorption in the CGM arises from galaxies that are fainter than L^{*} (Tumlinson & Fang 2005; Stocke et al. 2006; Prochaska et al. 2011b; Pratt et al. 2017). Since O VI has a cooling time of approximately 1 Myr (Gnat & Sternberg 2007), it acts as a clock for the formation of the CGM. This indicates that the low-ionization gas in the CGM of high-mass galaxies is a relic of an earlier, more mass-loaded, galactic outflow. The mass-loading of a 10^{7} K wind with cooler photoionized gas may enable the formation of the observed CGM.

7 SUMMARY

We searched for O VI in the six galaxies with far-ultraviolet coverage from MEGaSaURA. We found O VI in 3 of the 4 spectra with signal-to-noise ratios greater than 3 (Fig. 1). We then analyzed the interstellar absorption features in the spectrum of SGAS J122651.3+215220 (J1226+2152), a galaxy at a redshift of 2.926 ± 0.0002 that has the highest signal-to-noise ratio near the O VI 1032Å interstellar absorption line. We used the O VI line, which probes gas transitioning between warm (10^{4} K) and hot (>10^{7} K) temperatures, to study a seldom-probed phase of galactic outflows. The O VI has an observed column density of $10^{15.35\pm0.05}$ cm^{-2} (although it is likely saturated at the bluest velocities) and a maximum outflow velocity near -530 km s^{-1}. The maximum velocity is consistent with saturated low-ionization tracers like C II 1335Å and Si II 1260Å (Table 1). We found that the O VI line profile has two regimes: a low-velocity portion that closely resembles weaker low-ionization lines, and a high-velocity portion that resembles the strong saturated lines. The O VI line profile transitions between these two regimes at a velocity of −200 km s^{-1} (Fig. 4 and Fig. 6). The O VI and photoionized gas have similar velocity profiles and covering fractions, indicating that the two phases are co-spatial.

Using the Si IV doublet, we studied how the optical depth and covering fraction of low-ionization gas varies with velocity. We then corrected the observed Si IV column density for the covering fraction and found that the Si IV column density drops at velocities blueward of -200 km s^{-1}. After correcting the O VI column density for the Si IV covering fraction, the O VI column density rises at velocities blueward of -200 km s^{-1}. O VI is produced as the low-ionization gas is destroyed (Fig. 8).

We used five weak absorption lines to model the ionization structure of the outflow with CLOUDY photoionization models. We found that many of the low-ionization lines are adequately predicted by the photoionization models, but the models produce negligible O VI (see columns 6 and 7 in Table 1). Combined with the non-detection of the N V line (Fig. 7), we postulated that the O VI is created either through conductive evaporation of the photoionized gas by a hot outflow, or through a cooling flow between a hot outflow and the cooler photoionized gas. We used these two models to derive upper limits of the O VI ionization corrections (Section 6.1).

We calculated upper limits of the O VI mass outflow rate and found that it steadily rises at blue velocities (see Fig. 10). The maximum transitional mass outflow rate is at least 10-100 times lower than the maximum of the photoionized mass outflow rate, depending on the O VI ionization mechanism and saturation of O VI. This suggests that the photoionized gas dominates the mass outflow rate at the observed velocities, although the mass outflow rate of the transitional phase rises, and overtakes, the photoionized mass outflow rate at the bluest velocities (Fig. 11).

The O VI phase likely dominates the mass outflow rate at velocities above the escape velocity (Fig. 11). This high-velocity gas completely removes mass from the galaxy, however it is not typically probed by rest-frame ultraviolet and optical observations. If studies want to measure the amount of gas removed from galaxies, the hotter outflow phases must be considered.

Finally, we put forth a physical picture where the observed O VI traces the destruction of the photoionized outflow by conduction and the incorporation of the photoionized gas into an unobserved $>$ 10^{7} K wind (Fig. 12, Section 6.3). To satisfy conservation of mass, the sum of the mass outflow rate for all of the different phases must remain constant, implying that the mass outflow rate of the transitional and hot wind increases as the photoionized mass outflow rate decreases. This is exactly what we observed in Fig. 11. This also implies that the mass outflow rate of the unobserved hot wind is massive and increasing at the largest velocities. We speculated on the effect of incorporating low-ionization gas into a hot wind and the formation of the circum-galactic medium (Section 6.3.1).

These observations provide new evidence for which gas escapes the gravitational potentials of galaxies. The high-velocity outflow drives the depletion of gas within galaxies, and quantifying it is important to understand what drives the star formation histories of galaxies. Larger samples of rest-frame ultraviolet spectra of galaxies with $z > 2.5$ will constrain the amount of gas removed from galaxies by hot outflows. J1226+2152 is one of the brightest gravitationally lensed galaxies at these redshifts, and it required 12.4 hr of integration time on the 6.5 m Magellan telescope. Larger surveys must wait for $20 - 30$ m class telescopes. Furthermore, actually probing the elusive 10^7 K wind phase is the largest, and possibly most important, missing component of galactic outflows. Future X-ray observatories, with higher sensitivity and spectral resolution, will measure the hot wind in galaxies outside of the local universe, determining whether hot winds contain the majority of the outflowing mass that escapes galaxies.

ACKNOWLEDGMENTS

We thank the referee for a thoughtful read of the paper, and comments that strengthened the work.

Support for this work was provided by NASA through Hubble Fellowship grant #51354 awarded by the Space Telescope Science Institute, which is operated by the Association of Universities for Research in Astronomy, Inc., for NASA, under contract NAS 5-26555.

This paper has been typeset from a TEX/LATEX file prepared by the author.

REFERENCES

Allen M. G., Groves B. A., Dopita M. A., Sutherland R. S., Kewley L. J., 2008, ApJS, 178, 20
Arribas S., Colina L., Bellocchi E., Maiolino R., Villar-Martín M., 2014, A&A, 568, A14
Baldwin J. A., Ferland G. J., Martin P. G., Corbin M. R., Cota S. A., Peterson B. M., Slettebak A., 1991, ApJ, 374, 580
Ballet J., Arnaud M., Rothenflug R., 1986, A&A, 161, 12
Bordoloi R., et al., 2014, ApJ, 794, 130
Bordoloi R., Heckman T. M., Norman C. A., 2016a, preprint, (arXiv:1605.07187)
Bordoloi R., Rigby J. R., Tumlinson J., Bayliss M. B., Sharon K., Gladders M. G., Wuyts E., 2016b, MNRAS, 458, 1891
Borkowski K. J., Balbus S. A., Fristrom C. C., 1990, ApJ, 355, 501
Borthakur S., et al., 2015, ApJ, 813, 46
Brinchmann J., Charlot S., Heckman T. M., Kauffmann G., Tremonti C., White S. D. M., 2004, ArXiv Astrophysics e-prints,
Brüggen M., Scannapieco E., 2016, ApJ, 822, 31
Bustard C., Zweibel E. G., D'Onghia E., 2016, ApJ, 819, 29
Calzetti D., Armus L., Bohlin R. C., Kinney A. L., Koornneef J., Storchi-Bergmann T., 2000, ApJ, 533, 682
Cardelli J. A., Clayton G. C., Mathis J. S., 1989, ApJ, 345, 245
Chen Y.-M., Tremonti C. A., Heckman T. M., Kauffmann G., Weiner B. J., Brinchmann J., Wang J., 2010, AJ, 140, 445
Chevalier R. A., Clegg A. W., 1985, Nature, 317, 44
Chisholm J., Matsushita S., 2016, ApJ, 830, 72
Chisholm J., Tremonti C. A., Leitherer C., Chen Y., Wofford A., Lundgren B., 2015, ApJ, 811, 149
Chisholm J., Tremonti C. A., Leitherer C., Chen Y., Wofford A., 2016a, MNRAS, 457, 3133
Chisholm J., Tremonti Christy A., Leitherer C., Chen Y., 2016b, MNRAS, 463, 541
Chisholm J., Tremonti C. A., Leitherer C., Chen Y., 2017, MNRAS, 469, 4831
Cooper J. L., Bicknell G. V., Sutherland R. S., Bland-Hawthorn J., 2009, ApJ, 703, 330
Ferland G. J., et al., 2013, rmxaa, 49, 137
Fielding D., Quataert E., Martizzi D., Faucher-Giguère C.-A., 2017, MNRAS, 470, L39
Gnat O., Sternberg A., 2007, ApJS, 168, 213
Green G. M., et al., 2015, ApJ, 810, 25
Griffiths R. E., Ptak A., Feigelson E. D., Garmire G., Townsley L., Brandt W. N., Sambruna R., Bregman J. N., 2000, Science, 290, 1325
Grimes J. P., Heckman T., Hoopes C., Strickland D., Aloisi A., Meurer G., Ptak A., 2006, ApJ, 648, 310
Grimes J. P., et al., 2007, ApJ, 668, 891
Grimes J. P., et al., 2009, ApJS, 181, 272
Heckman T. M., 2002, in Mulchaey J. S., Stocke J. T., eds, Astronomical Society of the Pacific Conference Series Vol. 254, Extragalactic Gas at Low Redshift. p. 292 (arXiv:astro-ph/0107438)
Heckman T. M., Armus L., Miley G. K., 1990, ApJS, 74, 833
Heckman T. M., Lehnert M. D., Strickland D. K., Armus L., 2000, ApJS, 129, 493
Heckman T. M., Sembach K. R., Meurer G. R., Strickland D. K., Martin C. L., Calzetti D., Leitherer C., 2001, ApJ, 554, 1021
Heckman T. M., et al., 2011, ApJ, 730, 5
Heckman T. M., Alexandroff R. M., Borthakur S., Overzier R., Leitherer C., 2015, ApJ, 809, 147
Hopkins P. F., Kereš D., Oñorbe J., Faucher-Giguère C.-A., Quataert E., Murray N., Bullock J. S., 2014, MNRAS, 445, 581
Indebetouw R., Shull J. M., 2004, ApJ, 605, 205
Indriolo N., Geballe T. R., Oka T., McCall B. J., 2007, ApJ, 671, 1736
Jenkins E. B., 2009, ApJ, 700, 1299
Kauffmann G., et al., 2003, MNRAS, 341, 33
Klein R. I., McKee C. F., Colella P., 1994, ApJ, 420, 213
Koester B. P., Gladders M. D., Hennawi J. F., Sharon K., Wuyts E., Rigby J. R., Bayliss M. B., Dahle H., 2010, ApJ, 723, L73
Kwak K., Shelton R. L., 2010, ApJ, 719, 523
Lamers H. J. G. L. M., Cassinelli J. P., 1999, Introduction to Stellar Winds. Cambridge, UK: Cambridge University Press
Larson R. B., 1974, MNRAS, 169, 229
Leitherer C., et al., 1999, ApJS, 123, 3
Leitherer C., Li I.-H., Calzetti D., Heckman T. M., 2002, ApJS, 140, 303
Leitherer C., Ortiz Otálvaro P. A., Bresolin F., Kudritzki R.-P., Lo Faro B., Pauldrach A. W. A., Pettini M., Rix S. A., 2010, ApJS, 189, 309
Leroy A. K., et al., 2015, ApJ, 814, 83
Mac Low M.-M., McCray R., Norman M. L., 1989, ApJ, 337, 141
Madau P., Pozzetti L., Dickinson M., 1998, ApJ, 498, 106
Markwardt C. B., 2009, in Bohlender D. A., Durand D., Dowler P., eds, Astronomical Society of the Pacific Conference Series Vol. 411, Astronomical Data Analysis Software and Systems XVIII. p. 251 (arXiv:0902.2850)
Marshall J. L., et al., 2008, in Ground-based and Airborne Instrumentation for Astronomy II. p. 701454 (arXiv:0807.3774), doi:10.1117/12.789972
Martin C. L., 2005, ApJ, 621, 227
Martin C. L., Bouché N., 2009, ApJ, 703, 1394
Matsushita S., Kawabe R., Matsumoto H., Tsuru T. G., Kohno K., Morita K.-I., Okumura S. K., Vila-Vilaró B., 2000, ApJ, 545, L107
McKee C. F., Cowie L. L., 1977, ApJ, 215, 213
McKee C. F., Ostriker J. P., 1977, ApJ, 218, 148
Meynet G., Maeder A., Schaller G., Schaerer D., Charbonnel C., 1994, A&AS, 103, 97
Murray N., Quataert E., Thompson T. A., 2005, ApJ, 618, 569
Murray N., Martin C. L., Quataert E., Thompson T. A., 2007, ApJ, 660, 211
Oppenheimer B. D., Davé R., 2006, MNRAS, 373, 1265
Pettini M., Rix S. A., Steidel C. C., Adelberger K. L., Hunt M. P., Shapley A. E., 2002, ApJ, 569, 742
Pratt C. T., Stocke J. T., Keeney B. A., Danforth C. W., 2017, preprint, (arXiv:1706.05103)

Prochaska J. X., Kasen D., Rubin K., 2011a, ApJ, 734, 24
Prochaska J. X., Weiner B., Chen H.-W., Mulchaey J., Cooksey K., 2011b, ApJ, 740, 91
Prochaska J. X., et al., 2017, ApJ, 837, 169
Reyes R., Mandelbaum R., Gunn J. E., Pizagno J., Lackner C. N., 2011, MNRAS, 417, 2347
Rigby J. R., et al., 2017a, preprint, (arXiv:1710.07294)
Rigby J. R., et al., 2017b, preprint, (arXiv:1710.07499)
Rubin K. H. R., Prochaska J. X., Koo D. C., Phillips A. C., Martin C. L., Winstrom L. O., 2014, ApJ, 794, 156
Rupke D. S., Veilleux S., Sanders D. B., 2005a, ApJS, 160, 87
Rupke D. S., Veilleux S., Sanders D. B., 2005b, ApJS, 160, 115
Savage B. D., Sembach K. R., 1991, ApJ, 379, 245
Scannapieco E., Brüggen M., 2015, ApJ, 805, 158
Scarlata C., Panagia N., 2015, ApJ, 801, 43
Shapiro P. R., Benjamin R. A., 1991, PASP, 103, 923
Sharp R. G., Bland-Hawthorn J., 2010, ApJ, 711, 818
Shelton R. L., 1998, ApJ, 504, 785
Slavin J. D., Shull J. M., Begelman M. C., 1993, ApJ, 407, 83
Sobolev V. V., 1960, Moving envelopes of stars. "Cambridge: Harvard University Press"
Spitzer Jr. L., 1956, ApJ, 124, 20
Spitzer Jr. L., 1996, ApJ, 458, L29
Springel V., Hernquist L., 2003, MNRAS, 339, 312
Steidel C. C., Erb D. K., Shapley A. E., Pettini M., Reddy N., Bogosavljević M., Rudie G. C., Rakic O., 2010, ApJ, 717, 289
Stocke J. T., Penton S. V., Danforth C. W., Shull J. M., Tumlinson J., McLin K. M., 2006, ApJ, 641, 217
Strickland D. K., Heckman T. M., 2009, ApJ, 697, 2030
Strickland D. K., Stevens I. R., 2000, MNRAS, 314, 511
Suchkov A. A., Berman V. G., Heckman T. M., Balsara D. S., 1996, ApJ, 463, 528
Sutherland R. S., Dopita M. A., 1993, ApJS, 88, 253
Thompson T. A., Quataert E., Zhang D., Weinberg D. H., 2016, MNRAS, 455, 1830
Tremonti C. A., et al., 2004, ApJ, 613, 898
Tumlinson J., Fang T., 2005, ApJ, 623, L97
Tumlinson J., et al., 2011, Science, 334, 948
Veilleux S., Cecil G., Bland-Hawthorn J., 2005, ARA&A, 43, 769
Wakker B. P., Savage B. D., Fox A. J., Benjamin R. A., Shapiro P. R., 2012, ApJ, 749, 157
Walter F., et al., 2017, ApJ, 835, 265
Wang B., 1995a, ApJ, 444, 590
Wang B., 1995b, ApJ, 444, L17
Weaver R., McCray R., Castor J., Shapiro P., Moore R., 1977, ApJ, 218, 377
Weiner B. J., et al., 2009, ApJ, 692, 187
Weiß A., Walter F., Neininger N., Klein U., 1999, A&A, 345, L23
Werk J. K., et al., 2014, ApJ, 792, 8
Westmoquette M. S., Smith L. J., Gallagher III J. S., Trancho G., Bastian N., Konstantopoulos I. S., 2009, ApJ, 696, 192
White S. D. M., Frenk C. S., 1991, ApJ, 379, 52
Woosley S. E., Weaver T. A., 1995, ApJS, 101, 181
Wuyts E., Rigby J. R., Gladders M. D., Gilbank D. G., Sharon K., Gralla M. B., Bayliss M. B., 2012, ApJ, 745, 86